Geochemistry, Geophysics, Geosystems®

AGU ADVANCING EARTH AND SPACE SCIENCE

RESEARCH ARTICLE
10.1029/2021GC010213

Extent and Volume of Lava Flows Erupted at 9°50′N, East Pacific Rise in 2005–2006 From Autonomous Underwater Vehicle Surveys

Jyun-Nai Wu[1], Ross Parnell-Turner[1], Daniel J. Fornari[2], Gregory Kurras[3], Natalia Berrios-Rivera[1], Thibaut Barreyre[4], and Jill M. McDermott[5]

[1]Institute of Geophysics and Planetary Physics, Scripps Institution of Oceanography, University of California, San Diego, CA, USA, [2]Department of Geology and Geophysics, Woods Hole Oceanographic Institution, Woods Hole, MA, USA, [3]Seafloor Investigations LLC, Seattle, WA, USA, [4]Department of Earth Science, University of Bergen, Bergen, Norway, [5]Department of Earth and Environmental Science, Lehigh University, Bethlehem, PA, USA

Abstract Seafloor volcanic eruptions are difficult to directly observe due to lengthy eruption cycles and the remote location of mid-ocean ridges. Volcanic eruptions in 2005–2006 at 9°50′N on the East Pacific Rise have been well documented, but the lava volume and flow extent remain uncertain because of the limited near-bottom bathymetric data. We present near-bottom data collected during 19 autonomous underwater vehicle (AUV) *Sentry* dives at 9°50′N in 2018, 2019, and 2021. The resulting 1 m-resolution bathymetric grid and 20 cm-resolution sidescan sonar images cover 115 km^2, and span the entire area of the 2005–2006 eruptions, including an 8 km^2 pre-eruption survey collected with AUV *ABE* in 2001. Pre- and post-eruption surveys, combined with sidescan sonar images and seismo-acoustic impulsive events recorded during the eruptions, are used to quantify the lava flow extent and to estimate changes in seafloor depth caused by lava emplacement. During the 2005–2006 eruptions, lava flowed up to ~3 km away from the axial summit trough, covering an area of ~20.8 km^2; ~50% larger than previously thought. Where pre- and post-eruption surveys overlap, individual flow lobes can be resolved, confirming that lava thickness varies from ~1 to 10 m, and increases with distance from eruptive fissures. The resulting lava volume estimate indicates that ~57% of the melt extracted from the axial melt lens probably remained in the subsurface as dikes. These observations provide insights into recharge cycles in the subsurface magma system, and are a baseline for studying future eruptions at the 9°50′N area.

Plain Language Summary Volcanism on Earth primarily occurs in the oceans, at ridges where plates spread apart and molten rock intrudes the crust and erupts onto the seafloor. These eruptions frequently repave the seafloor and massively impact deep-sea ecosystems, but they remain poorly understood because the difficulties of collecting data in the deep ocean. We present meter-scale mapping of the volcanic system at the East Pacific Rise, 9°50′N, which erupted in 1991–1992 and 2005–2006, and is one of the best-studied hydrothermal vent areas. Using sonar data collected using underwater robots before and after the 2005–2006 eruptions, we identify the margins of lava flows that paved over the seafloor, and estimate their thickness and volume. Lava flowed as far as 3 km from the mid-ocean ridge, covering an area similar in size to Manhattan Island, NY. Using depth differencing between pre- and post-eruption surveys, we find that lava flows are, on average, ~1 m thick, and a total volume of 22.4 ± 7 × 10^6 m^3 erupted. The new, 1 m resolution bathymetric and 0.2 m resolution sidescan data provide a baseline that will be essential to study the next volcanic eruption at EPR 9°50'N, which is likely to happen in the coming few years.

Key Points:

- Near-bottom bathymetric and sidescan sonar data collected by autonomous underwater vehicle *Sentry* reveal meter-scale volcanic features at East Pacific Rise
- Flow margin identification shows that 2005–2006 lava extended over an area that is ~50% larger than previously mapped
- Volume of 2005–2006 eruptions was 22.4 ± 7 × 10^6 m^3, while 57% of total volume likely remained in the crust as dikes

Supporting Information:

Supporting Information may be found in the online version of this article.

Correspondence to:

J.-N. Wu,
wjyunnai@ucsd.edu

Citation:

Wu, J.-N., Parnell-Turner, R., Fornari, D. J., Kurras, G., Berrios-Rivera, N., Barreyre, T., & McDermott, J. M. (2022). Extent and volume of lava flows erupted at 9°50′N, East Pacific Rise in 2005–2006 from autonomous underwater vehicle surveys. *Geochemistry, Geophysics, Geosystems*, *23*, e2021GC010213. https://doi.org/10.1029/2021GC010213

Received 15 OCT 2021
Accepted 20 JAN 2022

Author Contributions:

Conceptualization: Jyun-Nai Wu, Ross Parnell-Turner
Data curation: Jyun-Nai Wu, Ross Parnell-Turner, Daniel J. Fornari, Gregory Kurras, Natalia Berrios-Rivera
Formal analysis: Jyun-Nai Wu
Funding acquisition: Ross Parnell-Turner, Daniel J. Fornari, Thibaut Barreyre, Jill M. McDermott
Investigation: Jyun-Nai Wu, Ross Parnell-Turner

1. Introduction

Although >75% of Earth's crust is generated by volcanism along the global mid-ocean ridge (MOR; Crisp, 1984), only a few tens of eruption events on MORs and submarine arcs have been documented (e.g., Chadwick et al., 2008, 2019; Rubin et al., 2012; and references therein), and of those, in only a handful of cases at MORs has the erupted volume been calculated (Caress et al., 2012; Chadwick et al., 1991, 2001; Clague et al., 2017; Colman et al., 2012; Feuillet et al., 2021; Sinton, 2002; Soule et al., 2007). The areal extent of seafloor volcanic eruptions provides important constraints on the pace of crustal accretion (Sinton & Detrick, 1992), lava flow dynamics (Chadwick et al., 2016; Fundis et al., 2010; Soule et al., 2012), and processes related to hydrothermal venting (e.g., Haymon et al., 1991, 1993). Determining the timing, volume and extent of deep-sea eruptions is

Methodology: Jyun-Nai Wu, Ross Parnell-Turner
Project Administration: Ross Parnell-Turner, Daniel J. Fornari
Supervision: Ross Parnell-Turner
Validation: Daniel J. Fornari
Visualization: Jyun-Nai Wu, Gregory Kurras, Natalia Berrios-Rivera
Writing – original draft: Jyun-Nai Wu
Writing – review & editing: Jyun-Nai Wu, Ross Parnell-Turner, Daniel J. Fornari, Thibaut Barreyre, Jill M. McDermott

difficult due to the temporal variability of eruption cycles (~tens to hundreds of years) and the remote location of MORs beyond the reach of most land-based monitoring systems. The volume and areal extent of an eruption is critical for evaluating magmatic processes such as the recurrence rate, which can be partly estimated by the area of lava flows on the seafloor (e.g., Pyle, 2015). Using near-bottom sonar data collected before and after the eruption, and acoustic data recorded during the final phase of the eruptions, we calculate the lava flow extent, volume, and inferred dike sizes associated with a series of eruptions that took place during 2005–2006 at 9°50′N on the East Pacific Rise (EPR).

Estimates of the spatial extent and lava flow thickness (and hence volume) of any given submarine eruption are hampered by difficulties in making direct, high resolution measurements before and after the event. Early pioneering studies used bathymetric data collected by ship-mounted sonars before and after eruptions (e.g., Chadwick et al., 1991; Fox et al., 1992), however the lower resolution of shipboard multibeam bathymetry meant that accurate volumetric estimates remained elusive. More recently, advances in autonomous underwater vehicle (AUV) technology have led to the capability of meter-resolution near-bottom bathymetric mapping. AUV surveys before and after the 2011 eruption at Axial Seamount on the Juan de Fuca Ridge enabled the first precise mapping of an underwater eruption (Caress et al., 2012). Although pre- and post-eruption near-bottom towed sidescan sonar and bottom photography were collected over the area impacted by the 2005–2006 eruptions at EPR 9°50′N (Fornari et al., 2004; Fundis et al., 2010; Soule et al., 2007), the lack of complete pre- and post-eruption near-bottom bathymetric data over the eruption area has hampered precise lava thickness estimates.

1.1. 9°50′N Study Area

Bounded to the north and south by the Clipperton and Siqueiros transform faults, respectively, the 9°50′N segment of the EPR has been studied for more than 30 years (e.g., Fornari et al., 2012 and references therein). Much of our understanding about hydrothermal systems, magma generation beneath fast-spreading ridges, and submarine volcanic process were derived from this MOR segment (e.g., Fornari et al., 1998; Harding et al., 1993; Haymon et al., 1991, 1993; Humphris et al., 1995; Macdonald & Fox, 1988; Orcutt et al., 1976; Tolstoy et al., 2006, 2008; Wright et al., 1995). The fast-spreading EPR between 9° and 10°N is comprised of a broad axial high capped by a ~10–20 m-deep axial summit trough (AST, Figure 1, Carbotte & Macdonald, 1992; Fornari et al., 1998). Based on seismic reflection data, an axial magma lens (AML) has been identified along ~85% of the ridge axis between the Clipperton and Siqueiros transform faults, at a mean depth of 1,640 m ± 300 m, although it is ~200 m shallower under the main eruption area from 9°40′N to 9°54′N (Aghaei et al., 2014; Canales et al., 2012; Carbotte et al., 2013; Detrick et al., 1987; Han et al., 2014; Marjanović et al., 2014, 2018; Mutter et al., 1988; Xu et al., 2014). The AML is likely to be the source of the two documented eruptions in this segment, one in 1991–1992 (Haymon et al., 1993) and most recently in 2005–2006 (e.g., Soule et al., 2007; Tolstoy et al., 2006).

Some debate remains about the exact timing of 2005–2006 eruptions. Po-disequilibrium dating, CO_2 concentrations in basalt glasses and time-series monitoring of hydrothermal vent temperatures suggest that eruptive phases began in summer 2005 and continued to January 2006 (Barreyre et al., 2022; Cowen et al., 2007; Rubin et al., 2006, 2008). In contrast, seismo-acoustic events have been interpreted as a single eruptive episode that was limited to just 30–48 hr commencing on 22 January 2006 (Tan et al., 2016; Tolstoy et al., 2006). These observations could be explained by early, possibly more subdued phases of volcanism not generating acoustic activity in summer 2005, followed by a more spatially extensive, acoustic source-generating eruption phase in January 2006. Seafloor conditions following the eruption were documented using near-bottom digital photography, towed 120 kHz sidescan sonar imagery, and rock sampling using the submersible *Alvin* (Fornari et al., 2012; Fundis et al., 2010; Soule et al., 2007, 2012). Based on visual comparisons between pre- and post-eruption sidescan sonar and photographic imagery, lava from the 2005–2006 eruption was estimated to be ~1.5 m thick on average, giving a total volume of $\sim 22 \times 10^6$ m^3 (Soule et al., 2007), an order of magnitude smaller than the 2011 and 2015 eruptions at Axial Seamount, but similar in scale when only considering channelized flows (Caress et al., 2012; Clague et al., 2017).

Here, we estimate the extent of the 2005–2006 eruptions using near-bottom 1 m-resolution bathymetric data and 30 cm-resolution 120 kHz sidescan sonar imagery collected using the AUV *Sentry* during three research cruises, which occurred in 2018–2021. We use the location of acoustic events recorded during the final eruption sequences (Tan et al., 2016) to help determine areal extent of lava flows, and calculate the erupted volume using thickness

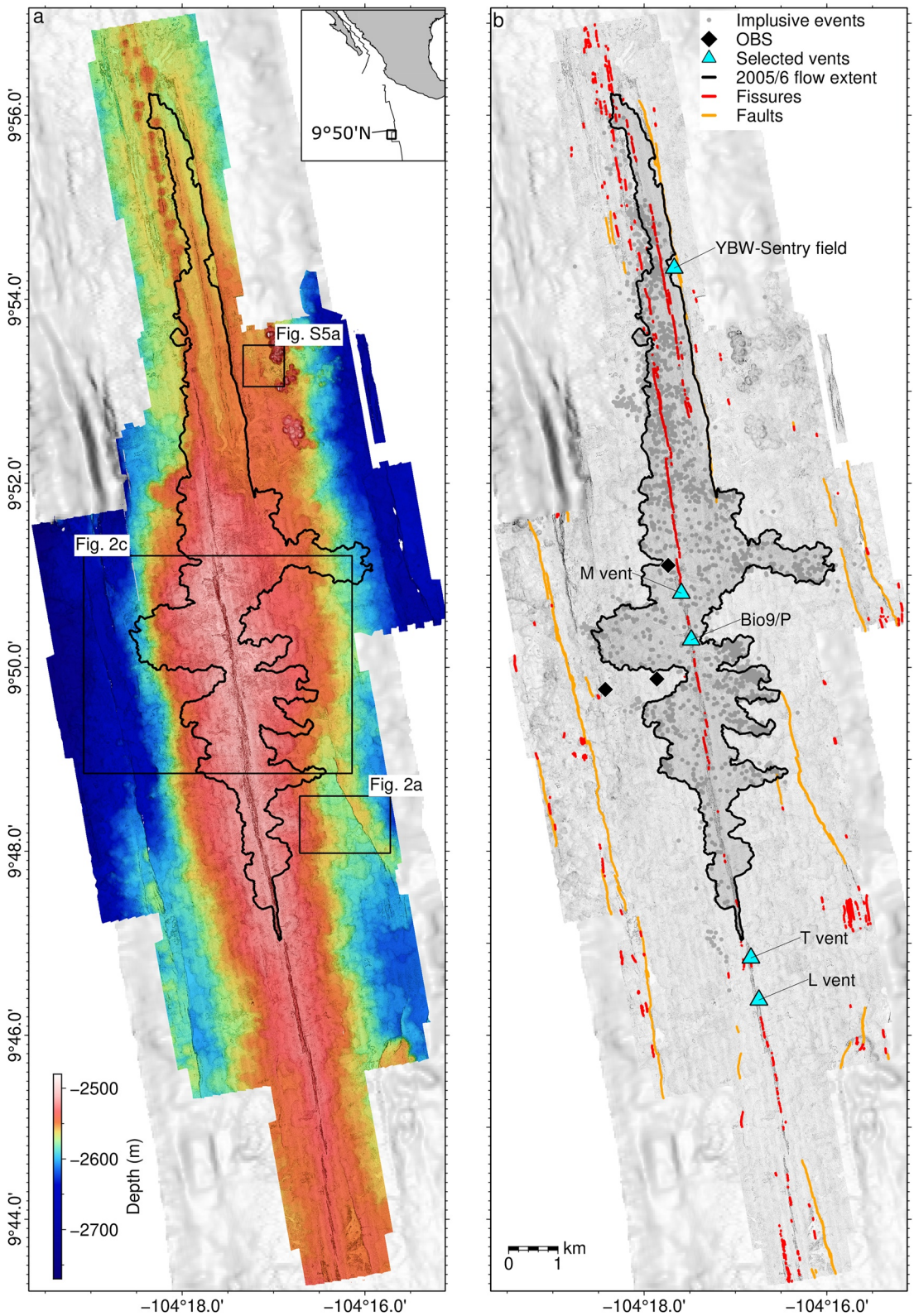

Figure 1.

Table 1
Position of Selected Hydrothermal Vent Sites at 9°50′N *Study Area*

Vent name	Latitude, °N	Longitude °E	Uncertainty[a]
YBW-Sentry[c]	9.9056382	−104.2945190	<5 m
Biovent	9.8493778	−104.2936035	<5 m
M Vent (north)	9.8466815	−104.2933190	<5 m
M Vent (south)[b]	9.8468151	−104.2934413	<5 m
Q Vent	9.8456579	−104.2931906	<5 m
East Wall	9.8418723	−104.2917846	<5 m
TeddyBear	9.8418328	−104.2919061	<5 m
Tica Vent	9.8399787	−104.2916175	<5 m
Bio9	9.8384848	−104.2913886	<5 m
P Vent	9.8379783	−104.2912484	<5 m
Lucky's mound[d]	9.7902200	−104.2870020	<10 m
V Vent	9.7878639	−104.2829768	<5 m
A Vent	9.7752718	−104.2802239	<5 m
Sentry spire[d]	9.7725580	−104.2870970	<10 m
L Hot8 Vent	9.7712382	−104.2790558	<5 m
L Vent	9.7709844	−104.2790402	<5 m
L diffuse	9.7711625	−104.2791328	<5 m

[a]Uncertainties estimated from ROV *Jason* USBL fixes, and from identification in *Sentry* bathymetric grid. [b]M vent includes multiple venting chimneys; M Vent (south) also named "Flea vent" elsewhere. [c]Active vent located a few hundred meters east of axial summit trough (AST). [d]Vents located a few hundred meters west of AST.

estimated from areas where *Sentry* bathymetric data overlap with a 5 m-resolution pre-eruption AUV *Autonomous Benthic Explorer* (*ABE*) bathymetric survey acquired in 2001 (Fornari et al., 2004). These new bathymetric and sidescan sonar data provide a baseline that will be essential for accurately determining the extent and volume of the next seafloor eruption at 9°50′N, and also allows us to obtain precise georeferenced positions for hydrothermal vents that are the focus of ongoing, decades-long monitoring efforts in this study area.

2. Data and Methods

A total of 19 AUV *Sentry* dives were conducted from R/V *Atlantis* and R/V *Roger Revelle* during three cruises in 2018 (AT42-06; two dives), 2019 (AT42-21; ten dives), and 2021 (RR2102; seven dives). Near-bottom multibeam bathymetric data were collected along track lines spaced 170 m apart, at ∼65 m above bottom, with a Reson 7125 system in 2018, and a Kongsberg EM2040 system in 2019 and 2021. Both bathymetric systems operate at 400 kHz, while 120 kHz sidescan data were collected simultaneously with an EdgeTech 2200-M in 2018, 2019, and an EdgeTech 2205 system in 2021. *Sentry*'s navigational position was obtained using a 300 kHz Teledyne Doppler velocity log (DVL) and a Sonardyne AvTrak2 ultra-short baseline (USBL) acoustic positioning system, combined with an iXblue Phins inertial navigation system (INS), and a Paroscientific 8B7000-I Digiquartz depth sensor. The resulting continuously mapped region extends 25.6 km along-axis and up to 8.0 km across-axis at its widest point near 9°50′N, covering a total of 115 km^2, from 9°43′N to 9°57′N (Figure 1).

2.1. AUV Navigation

Accurate AUV navigation is critical for repeat bathymetric surveys, allowing seamless merging of adjacent survey lines and co-registration of missions completed over multiple years, in order to resolve subtle changes in seafloor depth. Obtaining this level of precision is challenging because global navigation satellite system (GNSS) signals do not penetrate water. Final AUV positions were determined by joint integration of DVL and USBL fixes. A detailed discussion on vehicle navigation can be found in the Supporting Information. Final absolute navigational accuracy is estimated to be <10 m, assessed by comparing the position of seafloor features identified in the AUV bathymetric data with those visited by ROV *Jason,* whose position is resolved with an accuracy of <5 m.

3. Results

We mapped the EPR and its flanks from 9°43′ to 9°57′N primarily to cover the previously interpreted extent of: the area covered by 2005–2006 eruptions (Fundis et al., 2010; Soule et al., 2007), the 1991–1992 eruptions area, known hydrothermal vents (Table 1), and major bounding normal faults on off-axis flanks (e.g., Fornari et al., 2012; Haymon et al., 1993). The survey is also coincident with an 8 km^2 near-bottom scanning altimeter bathymetric survey collected using AUV *ABE* in 2001, and with near-bottom towed DSL120a sidescan sonar data collected in 2001 and 2007 (Figures 2c and 2d, Fornari et al., 2004; Soule et al., 2007). Cross-axis coverage extends up to ∼4 km away from the AST, including portions of the youngest normal fault on both flanks

Figure 1. (a) 1 m-resolution bathymetric data collected with Reson AUV3 (cruise AT42-06; 2018) and Kongsberg EM2040 (cruise AT42-21; 2019) multibeam echosounders mounted on AUV *Sentry*; gray shaded relief is 30 m-resolution shipboard data from cruise TN188 (White et al., 2006); boxes show locations of Figures 2a, 2b, and Figure S5a in Supporting Information S1. Inset: black box shows study site; thin black lines are plate boundaries. (b) Gray dots are impulsive events and black diamonds are locations of ocean bottom seismometer (OBS) that recorded data from 2005 to 2006 (Tan et al., 2016; Tolstoy et al., 2006); labeled blue triangles are selected hydrothermal vents; thin black line is 2005–2006 flow extent (this study); orange lines are faults, red lines are fissures.

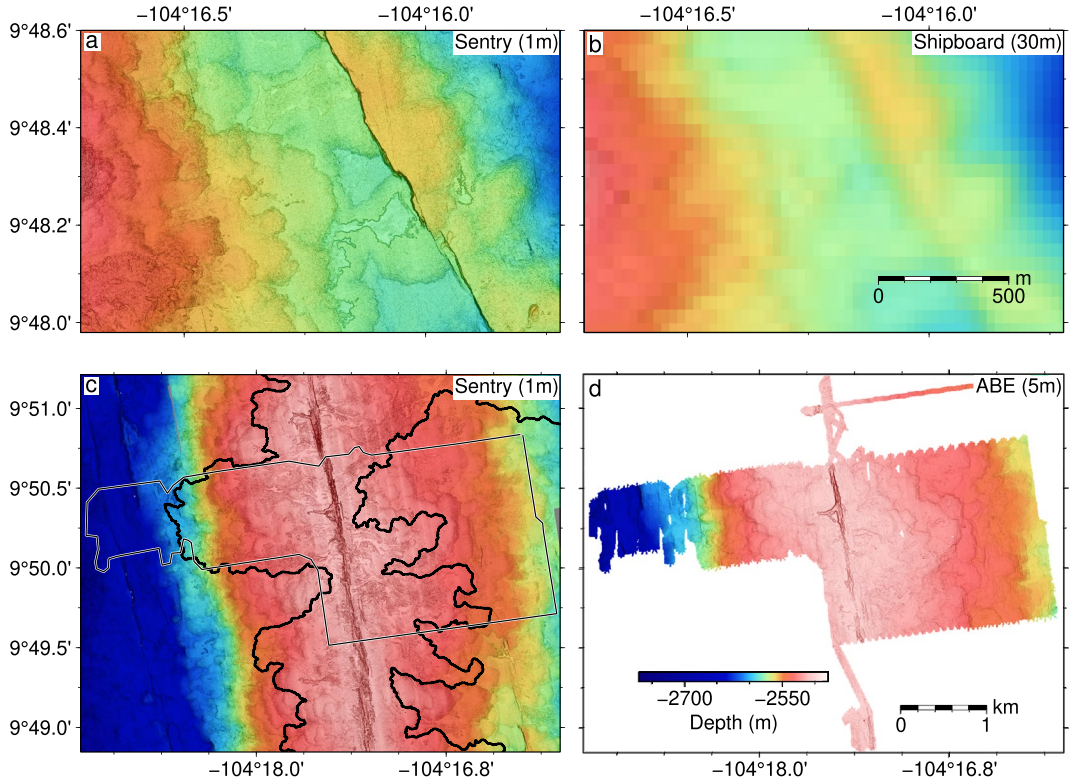

Figure 2. (a) 1 m-resolution bathymetric data collected by *Sentry* in 2019 (AT42-21) over fault scarp east of axial summit trough (AST) (location shown in Figure 1). (b) 30 × 50 m resolution bathymetric data collected over same fault using hull-mounted EM300 in 2005 (White et al., 2006). (c) 1 m-resolution bathymetric data collected by *Sentry* over area mapped by AUV *ABE* in 2001 (location shown in Figure 1); black polygon shows footprint of AUV *ABE* survey, acquired in 2001 during cruise AT07-04 (Fornari et al., 2004); black outline shows extent of 2005–2006 flows. (d) 5 m-resolution bathymetric data collected with an Imagenex 881 scanning sonar mounted on AUV *ABE* in 2001 (Fornari et al., 2004).

(Figure 1 and Figures 2a and 2b). Our results resolve seafloor volcanic and tectonic features in unprecedented detail, including lava flows, collapses (Figures 2a and 2b), fissures, lava channels, coalesced vent chimneys, and fault scarps (Figures 1b and 3).

3.1. Areal Extent and Thickness of 2005–2006 Eruptions

Distinguishing the spatial extent of lava flows from individual eruptions (Figure 4) is challenging due to subtle morphological definition of flows separated in age by several decades, but is essential to understand the history of magmatism (e.g., Wilcock et al., 2018). Previous studies at EPR 9°50′N used deep-towed sonar and photographic images to identify the contacts between the 2005–2006 eruptions and older lava flows, but these efforts were limited by survey coverage, and did not include extensive near-bottom bathymetric surveys (Fundis et al., 2010; Soule et al., 2007). We revised the 2005–2006 flow extent by comparing new bathymetric and sidescan sonar data with pre-eruption bathymetric and sidescan sonar images collected in 2001 (Fornari et al., 2004). In addition, the impulsive acoustic events (thought to arise due to cracking of rapidly cooled lava) recorded during the 2006 eruption phase (Tan et al., 2016) were used to help identify newly formed lava fronts. Due to the recording network geometry, impulsive event locations uncertainty in positions outside of the network is likely to be increased, with error ellipses largest in the east-west direction. As a result of this uncertainty, we only use the impulsive event locations as an indicative guide for flow extent identification, rather than as a strict criterion. Lava flow extent was defined based on six constraints, as follows. First, flow margins were defined by the bathymetric depth difference between 2001 pre-eruption *ABE* and 2018–2021 post-eruption *Sentry* bathymetric surveys (Figures 5–7). Second, subtle discontinuities in seafloor slope associated with flow margins (Figure 6c), and third, new volcanic constructs including lobate and channelized flows, collapses, changes in seafloor texture such as hackly flows, that appear in the 2018–2021 sidescan data but not in the 2001 sidescan data (Figure 3). Fourth, volcanic and

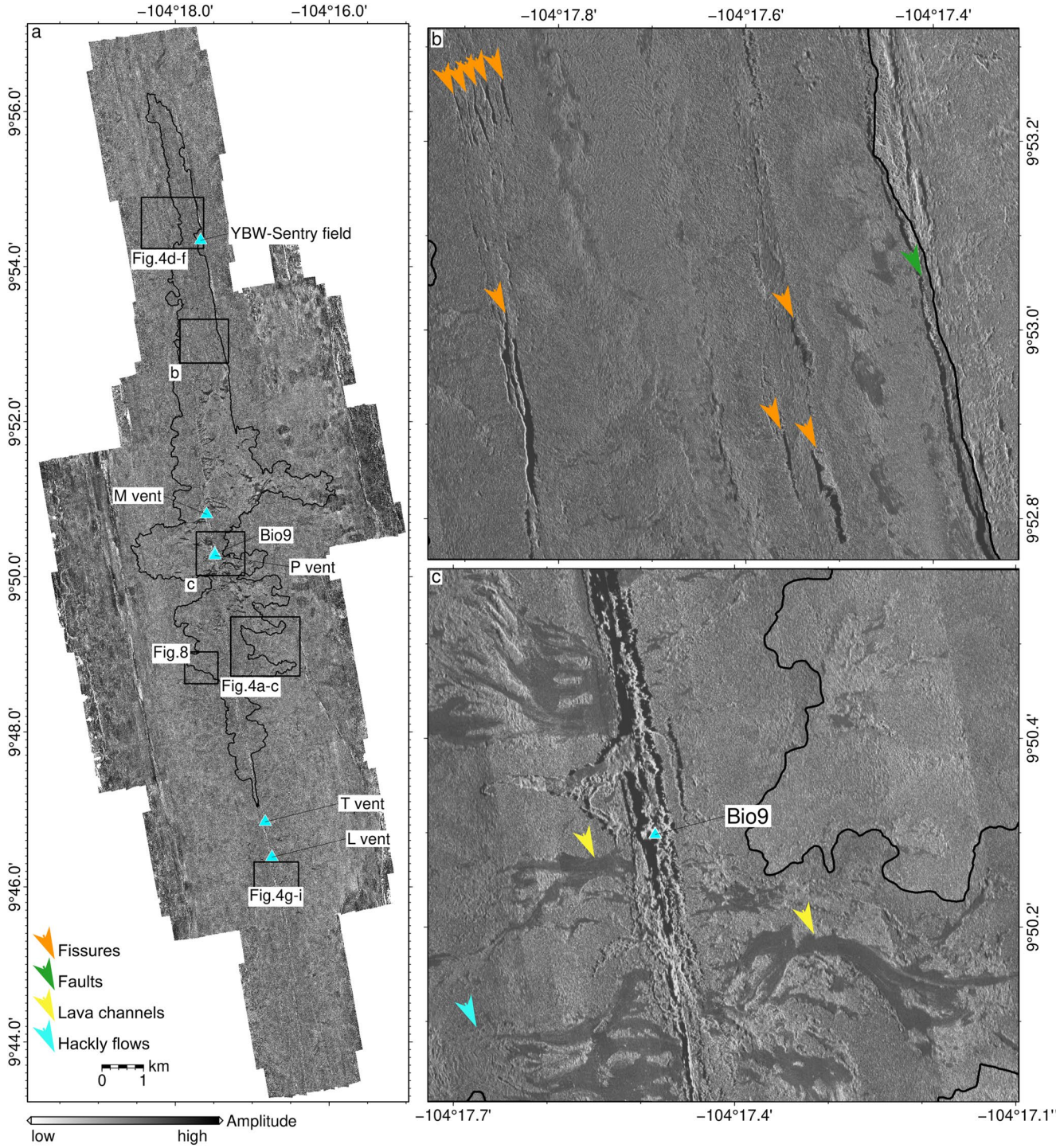

Figure 3. (a) 30 cm-resolution sidescan imagery collected with EdgeTech 2200m sonar operating at 120 kHz mounted on AUV *Sentry* in 2018–2021 (cruises AT42-06, AT42-21 and RR2102). Blue triangles are selected hydrothermal vents; thin black line is 2005–2006 flow extent. (b) Example sidescan imagery showing fissures (orange arrows) and faults (green arrows), location shown in (a). (c) Example sidescan imagery near axial summit trough (AST); showing lava channels (yellow arrows) and hackly flow (blue arrow).

tectonic relationships, such as collapses which have been infilled by later flows, or lobes that apparently flowed over fault scarps (Figures 4c and 4f). Fifth, areas that were clearly not re-paved by the 2005–2006 eruptions that were identified by correlating seafloor features visible in both the 2001 and 2018–2019 sidescan sonar images (Figure 4), and sixth, the location of impulsive events associated with lava-seawater interaction (described below;

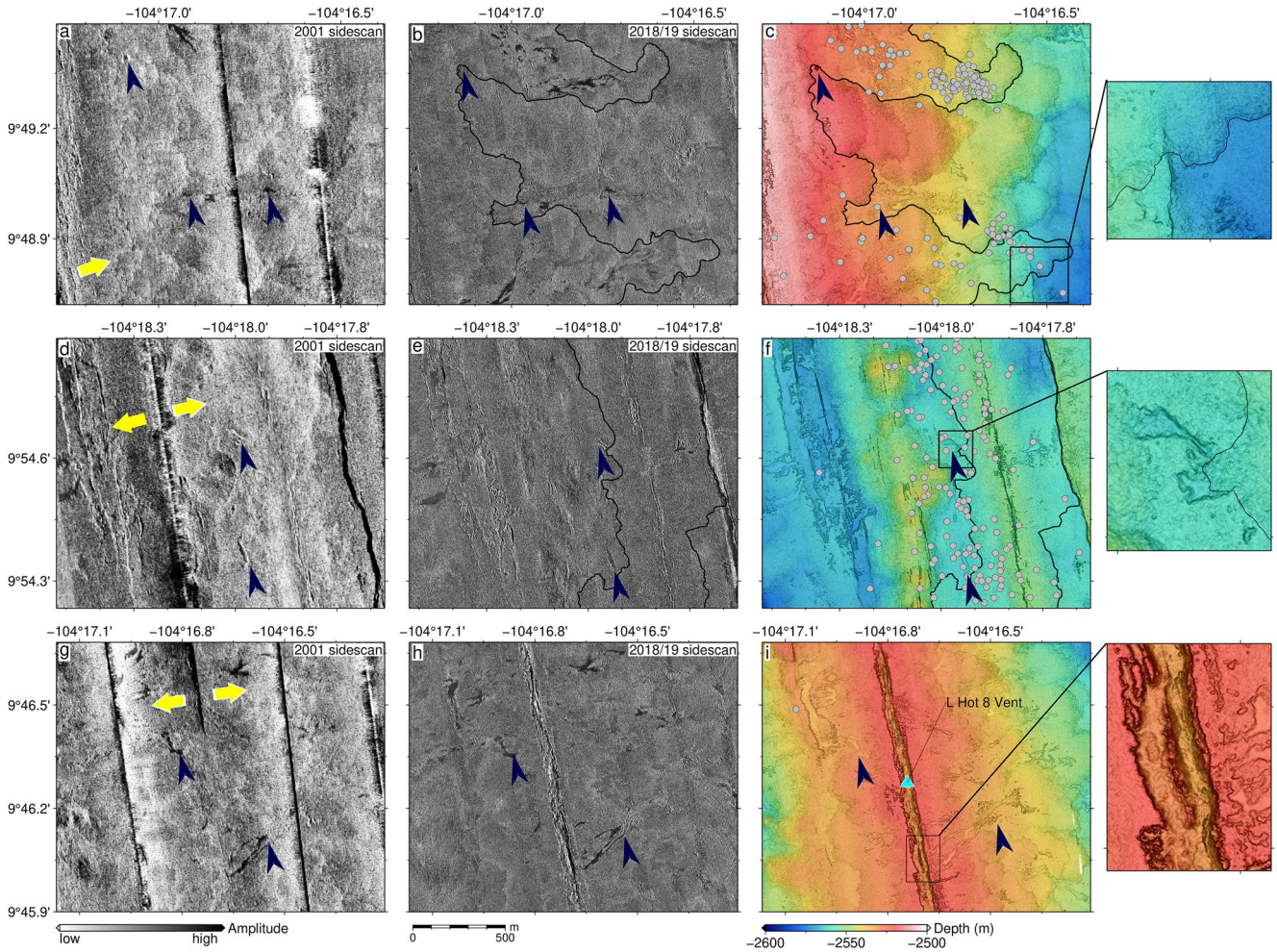

Figure 4. Comparison of sidescan images acquired before and after the 2005–2006 eruption (locations shown in Figure 3a); black arrows show seafloor features visible both pre- and post-eruption. (a and b) and (d and e) and (g and h): Sidescan images acquired with towed DSL120A sonar (cruise AT07-04, 2001 [Fornari et al., 2004]) and with EdgeTech 2200m on *Sentry* (cruise AT42-21, 2019), respectively. Gray dots are impulsive events (Tan et al., 2016); thin black line is 2005–2006 flow extent. Examples of lava flow over fault scarps, collapses infilled by lava flows, and linear fissure within axial summit trough (AST) in insect map of (c), (f), and (i), respectively.

Tan et al., 2016). Three examples of the approach to flow margin interpretation based upon different available observations are given in Figures 6–8.

Flow extent and thickness were determined from the bathymetric difference between pre- and post-eruption surveys, following the approach used at Axial Seamount (Caress et al., 2012). The 2018–2021 *Sentry* surveys were down-sampled to 5 m grid node spacing, and co-registered with the 2001 *ABE* data, by cross-correlating the two gridded datasets over a patch of seafloor outside of the interpreted 2005–2006 flow extent (Figures 5a–5c). *ABE* bathymetric data were then shifted 4.2 m vertically downward in order to obtain a maximum correlation coefficient. The bathymetric difference between the two co-registered grids was calculated, revealing the lava flow extent and thickness (mean = 1.2 m). These results are in good agreement with the location of impulsive events from January 2006 (Figure 5d). The resulting bathymetric difference grid covers three lava lobes that extend 2 km east of the AST, and one lava flow that extends 3 km west of the AST (Figure 5d).

At distances <400 m from the AST, the mean lava flow thickness is 0.9 m, which is thinner than in areas >400 m from the AST, where mean thickness is 1.9 m (Figure 9). Lava flow fronts on the eastern flank are up to ~4 m thick (Figure 6a), and up to ~9 m thick on the western flank (Figure 5d). In areas without pre-eruption bathymetric coverage, we define the 2005–2006 eruptions outline based upon the outermost lava front associated with

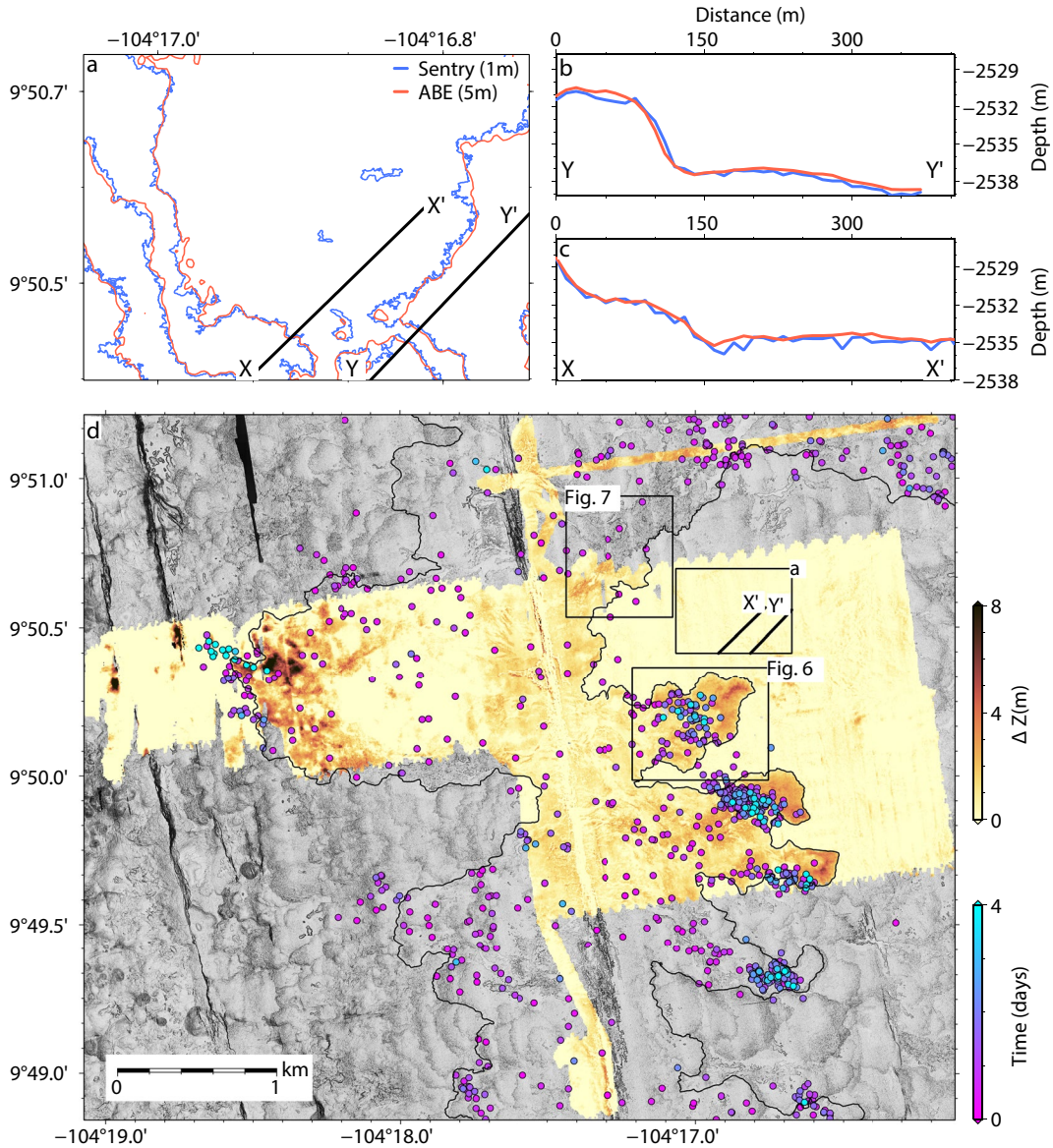

Figure 5. (a) Contours showing comparison of bathymetric data collected outside of 2005–2006 eruption extent. Red lines are pre-eruption data collected using *ABE* in 2001; blue lines are post-eruption data collected by *Sentry* in 2019. (b and c) Bathymetric profiles illustrating co-registration between shifted *ABE* and *Sentry* data. (d) Bathymetric difference map between pre- (*ABE*) and post- (*Sentry*) 2005–2006 eruptions surveys. Dots are impulsive events shaded by time after 2006-01-22 16:47 UTC (Tan et al., 2016), highlighting propagation toward the distal end of each flow away from the axial summit trough (AST). Mean flow thickness is 1.0 m, and up to ~9.0 m in the area ~2.0 km west of the AST near 9°50.4′N.

impulsive events, and following the principle of superposition, requiring that pre-eruption features visible in sidescan data must not have been covered up by 2005–2006 lava flows (Figure 8).

Acoustic impulsive events (n = 1,965) were detected by three ocean bottom seismographs (OBSs) between 22 and 29 January 2006, which are attributed to lava reaching the seafloor and flowing away from eruptive vents (Tan et al., 2016, Figure 1b). The spatiotemporal distribution of these events is consistent with lava lobes identified using sidescan sonar and towed deep-sea camera photographic imagery between 9°49′ and 9°52′N (Soule et al., 2007; Fundis et al., 2010), and *Sentry* bathymetric data from this study (Figures 1b, 4a, and 4b). The seafloor acoustic events could be generated either by explosions associated with magma degassing (e.g., Vergniolle et al., 1996), or by cracking as lava is quenched by seawater (e.g., Perfit et al., 2003), or implosions within lobate-sheet flow after molten lava has drained out (e.g., Chadwick et al., 2016). Impulsive events and lava flow

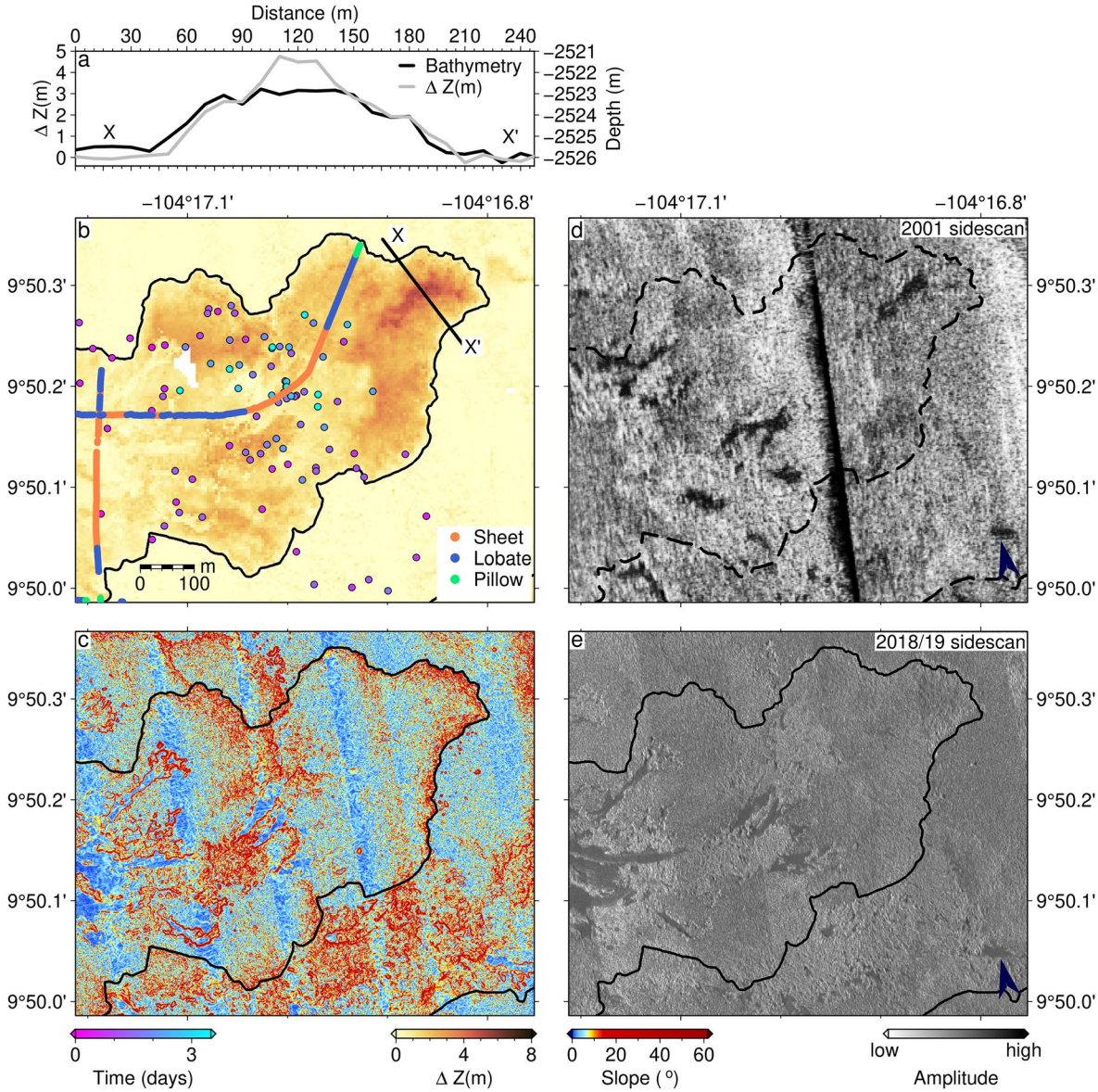

Figure 6. (a) Profiles of bathymetry (as observed using *Sentry* post-eruption), and bathymetric difference (ΔZ) between pre- and post-eruption surveys, across a lava flow lobe east of axial summit trough (AST). (b) Bathymetric difference map, showing definition of 2005–2006 flow margin (location shown in Figure 5); circles are impulsive events shaded by time after 2006-01-22 16:47 UTC (Tan et al., 2016); impulsive events outside of flow area could be mis-located; black line is 2005–2006 flow extent; shaded tracklines are lava morphology interpreted from near-bottom towed photographic images (Fundis et al., 2010). (c) Bathymetric slope, used to aid definition of flow margins. (d) Sidescan sonar image acquired pre-eruption (Fornari et al., 2004); dashed line is 2005–2006 flow extent. (e) Sidescan image acquired post-eruption; black/gray arrows show sheet flow and hackly flow front, respectively, visible both pre- and post-eruption.

termini are co-located in areas within ~3.5 km of the OBS locations, but agreement deteriorates at distances >4 km north and south of the network, where event locations appear to be biased to the west, likely due to the small number of instruments all of which were positioned west of the AST (Figure 1b). Hence, we consider the uncertainty of acoustic impulsive event locations to be greater at distances >4 km from the OBSs, and therefore rely on the bathymetric and sidescan sonar data to define the 2005–2006 eruption extent in these areas.

While the seismo-acoustic events indicate that a significant eruption phase occurred in January 2006 (Tan et al., 2016), Po-dating data of rock samples suggests two or three eruption phases occurring during summer and fall 2005 to January 2006 (Rubin et al., 2008), which is corroborated by anomalies in fluid temperature time-series recorded at M vent located within the AST near 9°51′N (Barreyre et al., 2022). Although our data reveal the detail seafloor features potentially showing different flow episodes (Figure 4f), we cannot reliably distinguish

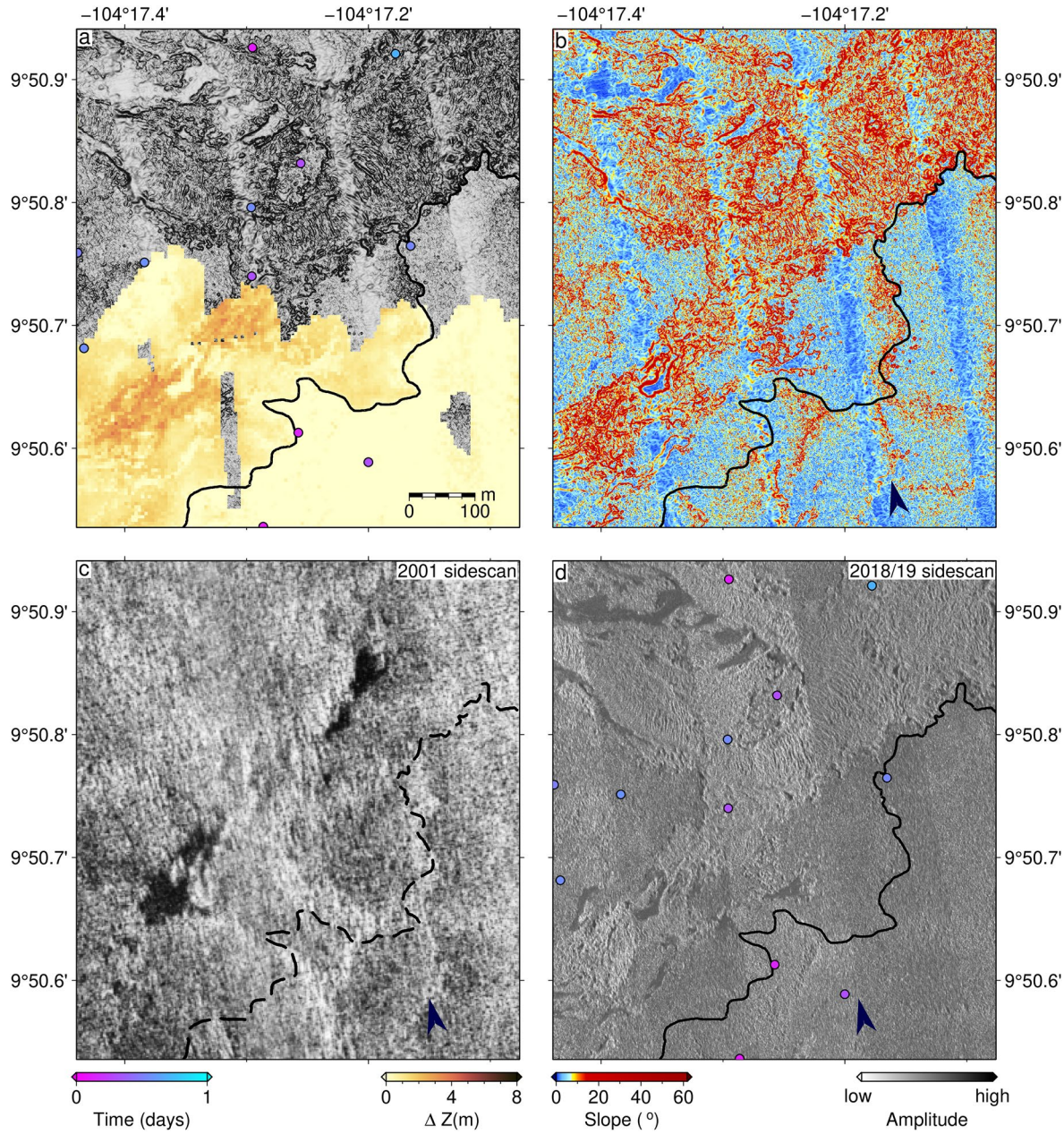

Figure 7. (a) Bathymetric difference between pre- and post-eruption surveys plotted on gray-shaded 1-m *Sentry* bathymetric data, showing multiple intersecting sheet flows from the 2005–2006 eruptions (location shown in Figure 5); black line is 2005–2006 flow extent; dots are impulsive events shaded by time after 2006-01-22 16:47 UTC (Tan et al., 2016). (b) Bathymetric slope, highlighting flow margins. (c) Sidescan sonar image acquired pre-eruption (Fornari et al., 2004); dashed line is 2005–2006 flow extent. (d) Post-eruption sidescan sonar image; black arrow shows seafloor feature visible both pre- and post-eruption. Solid black line is 2005–2006 flow margin from (a).

between these temporally. Therefore, our estimates of eruption volume represent an overall total, including all potential 2005–2006 eruption phases.

Combining these observations, lava flows from the January 2006 phase of the 2005–2006 eruptions traversed a few hundred meters to ~3 km away from the AST, and over an along-axis distance of ~17 km, yielding a total area of 20.8 km^2. North of 9°52.5′N, we identify two parallel fissure systems, both of which appeared to have been a source for new lava during the 2005–2006 eruptions. Although mapping data do not resolve new flows associated with the 2005–2006 eruption south of 9°47′N, basaltic lavas likely erupted in 2005–2006 were recovered from within the AST near 9°46.5′N (e.g., sample AL4205-3), suggesting that a localized eruption could have

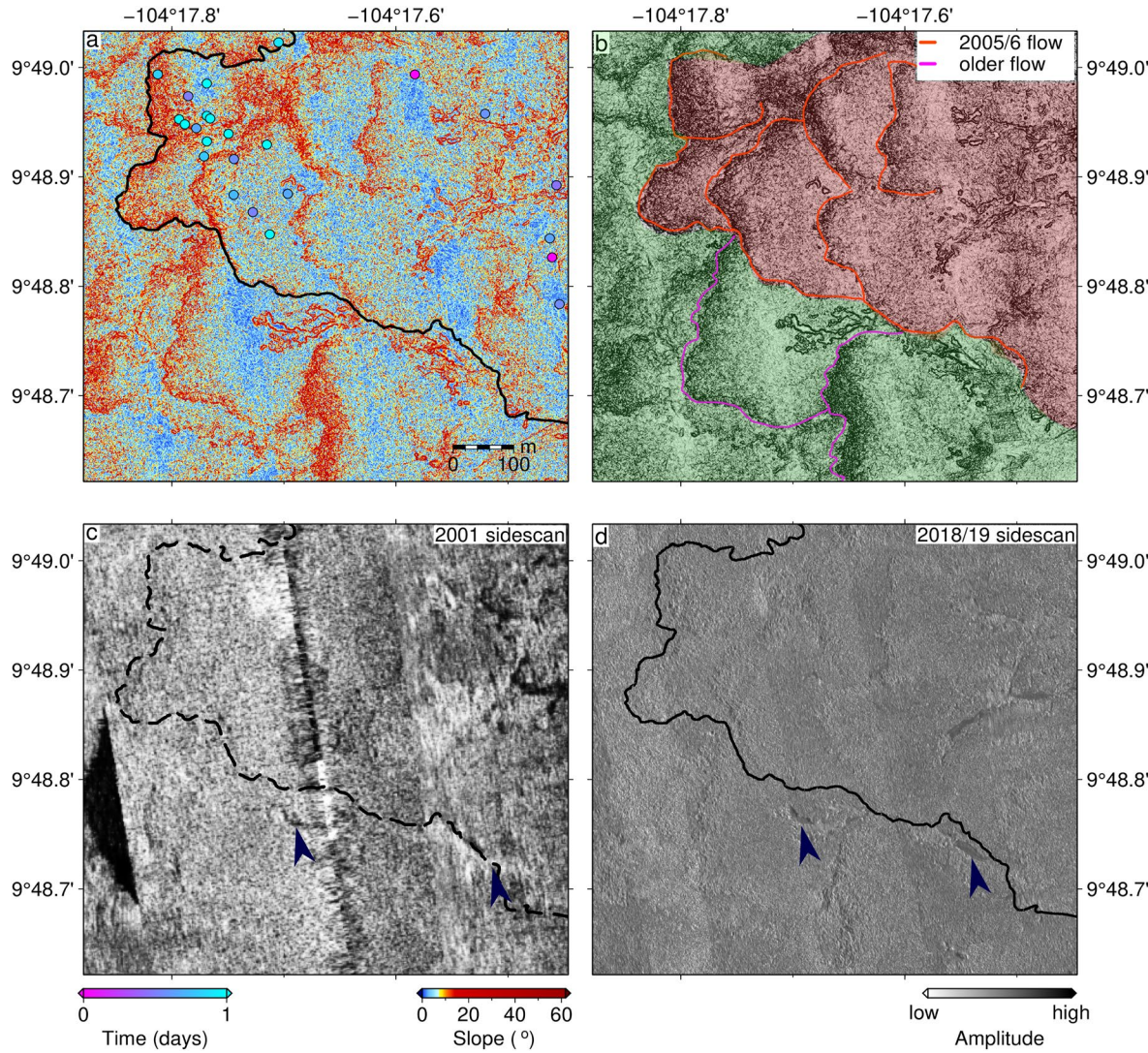

Figure 8. (a) Bathymetric slope, highlighting sequence of overlapping lobate flow margins west of axial summit trough (AST) (location in Figure 3); black line is 2005–2006 flow extent; dots are impulsive events shaded by time after 2006-01-22 16:47 UTC (Tan et al., 2016), which help identify 2005–2006 lobate flows. (b) Gray-shaded slope with interpretation of 2005–2006 lobates (red line/shading) and an older generation of flow fronts (magenta lines/green shading). (c) Sidescan sonar image acquired pre-eruption (Fornari et al., 2004); dashed line is 2005–2006 flow extent. (d) Post-eruption sidescan sonar image; black arrows show example seafloor features visible both pre- and post-eruption. Solid black line is 2005–2006 flow margin from (a).

occurred there (Goss et al., 2010). The 2005–2006 flows are bounded by normal faults on both flanks, and appear to have been deflected along the footwall of inward facing fault scarps (Figure 1).

3.2. Hydrothermal Vent Locations

Reliable identification and accurate positional information about individual hydrothermal vent sites are important for repeat, multidisciplinary observations of the seafloor hydrothermal processes and ecosystems occurring in the EPR 9°50′N study area. Ensuring that any single vent site is repeatedly visited over several years can be uncertain due to the rapidly changing geometry and growth/collapse of seafloor constructs and chimneys, evolving faunal populations, similarity between nearby structures, and lack of a consistent USBL-navigated vent location database. Several efforts to address these issues have been made using deep-towed camera and submersible surveys, seafloor benchmarks, and long baseline acoustic navigation (Ferrini et al., 2007; Fornari et al., 2004, 2012; Haymon et al., 1993; Soule et al., 2008). Prior to 2021, however, vent locations have not been constrained using spatially extensive near-bottom multibeam bathymetric data. Many of the known vent sites were revisited in

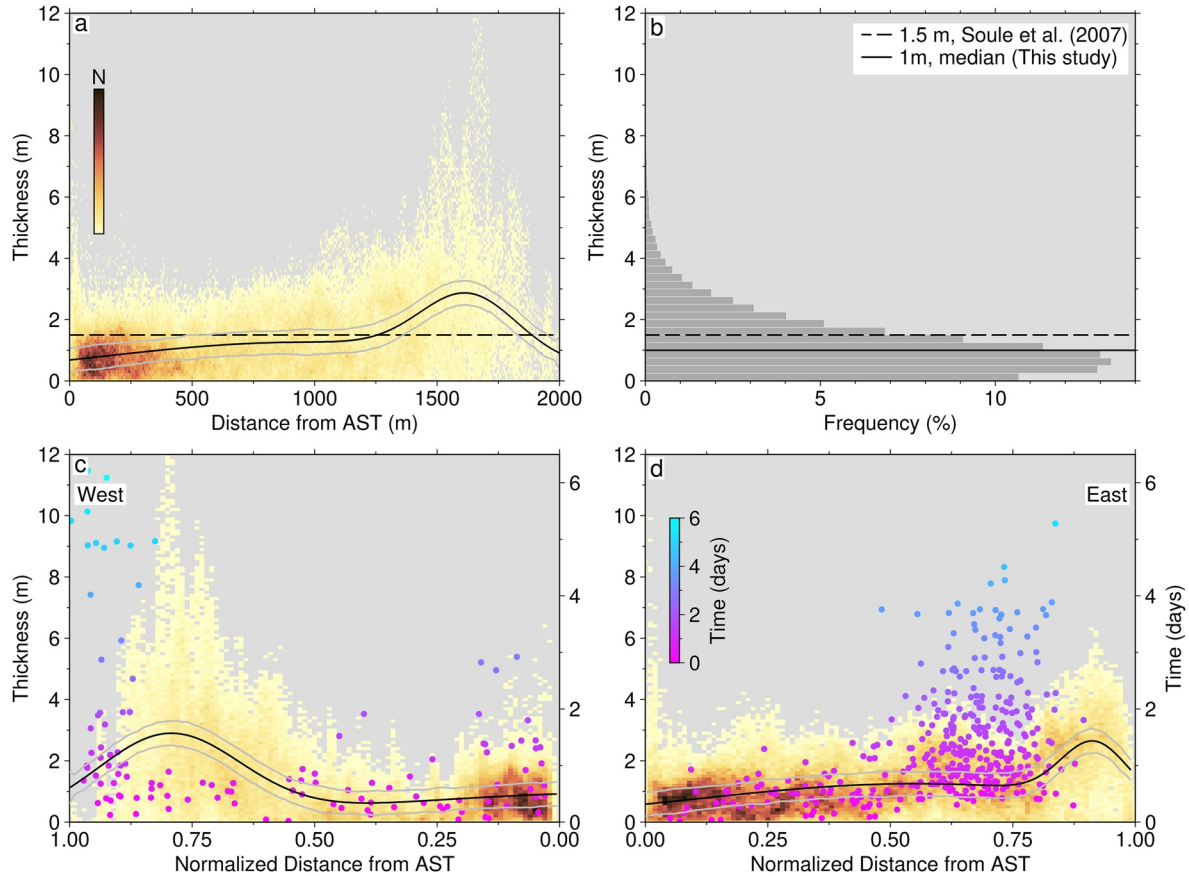

Figure 9. (a) 2005–2006 flow thickness (i.e., bathymetric difference between pre-eruption *ABE* and post-eruption *Sentry* surveys) as a function of distance from axial summit trough (AST), colors are normalized grid node density; black/gray line is second degree Gaussian function with 1σ error band; dashed lined is 1.5 m thickness assumed by Soule et al. (2007). (b) Flow thickness histogram; solid line is median (1 m, this study); dashed line is 1.5 m. (c and d) Flow thickness as a function of normalized distance from AST to edges of lava flows on west and east flank, respectively; dots are impulsive events shaded by time after 2006-01-22 16:47 UTC (Tan et al., 2016).

the 9°50′N area with ROV *Jason* during cruise RR2102 in 2021 for biological, geochemical, and geological sampling, occupying each site for >1 hr in many cases. The USBL navigational solutions from *Jason* during operations such as vent fluid sampling, temperature logger deployment, or instrument recovery were used to refine positions for these sites by taking the arithmetic mean from normally distributed location fixes, with accuracy better than ~5 m (Table 1). Many other previously documented vent sites, which were not revisited with *Jason* in 2021, are identifiable in the *Sentry* multibeam bathymetric grid, hence those locations were also able to be revised and documented to an accuracy better than ~10 m (Table 1).

4. Discussion

Lava flow thickness derived from bathymetric difference analysis between pre- and post-eruption surveys shows a trend of thickening from 0.8 to 1.7 m toward the distal end of flow lobes (Figure 9). This trend is in good agreement with observations from photographic images showing that sheet and lobate flow morphologies are prevalent in areas proximal to the AST, while pillow flows are more commonly found toward distal flow margins (Fundis et al., 2010). Generally, lava surface morphology transitions from sheet to lobate flows away from the AST toward flow termini, coinciding with a progressive increase in flow thickness. The final transition from lobate to pillow morphology near flow margins usually occurs over very short distances of just several meters, coinciding with lava flows up to 4 m thick (Figure 6b).

4.1. Volumetric Estimate of 2005–2006 Eruptions

We estimate the total volume of lava erupted by combining the areal extent estimate of the 2005–2006 eruptions (20.8 km^2) with thickness constraints from areas of repeat bathymetric surveys, pre- and post-eruption. Within the repeat survey area, we extracted profiles of flow thickness spaced every 10 m along-axis, oriented parallel to plate spreading direction (085°). We fitted a second-degree Gaussian function to these flow thickness profiles on each side of the axis independently (Figure 9a), and then normalized each Gaussian fit function with respect to across axis eruption width (i.e., distance from AST to flow extent maxima) to mitigate the uncertainty that arises due to flow length, yielding

$$y(d) = \sum_{i=1}^{2} a_i \ \exp - \left(\frac{d - \mu_i}{\sigma_i} \right)^2, \tag{1}$$

where y is the thickness, d is normalized distance from the AST, a is the amplitude function, and μ and σ are scaling factors. Multiplying this thickness function by our estimate of eruption area yields a revised eruption volume of $22.4 \pm 7 \times 10^6$ m^3.

Previous estimates of the volume of the 2005–2006 eruptions were based on a flow extent of 14 km^2, defined from sidescan sonar and photographic imagery, combined with an assumed constant 1.5 m flow thickness, yielding a volume estimate of 22×10^6 m^3 (Soule et al., 2007). While the two estimates are close in total volume, we find the areal extent to be ∼50% greater (Figure S1 in Supporting Information S1), suggesting the 2005–2006 flows were thinner and more spatially extensive than previously thought. This volume estimate assumes that the area of the pre- and post-eruption AUV surveys is representative of typical flow thickness, which cannot be verified without independent estimates of flow thickness in other areas.

Impulsive acoustic events are likely to be generated by either implosions of molten lava or interaction between lava with seawater which could provide insights into lava flow dynamics (e.g., Chadwick et al., 2016; Engels et al., 2003; Perfit et al., 2003; Tan et al., 2016; Wilcock et al., 2016). Flow margins east of the AST (where repeat AUV bathymetric data allow precise identification) coincide with locations of impulsive events that occurred 0.5–4.5 days after the January 2006 eruption phase (Tan et al., 2016, Figure 9d). Impulsive events are clustered at distances ∼100–300 m proximal to the AST from mapped flow margins, that is, not at the edge of the flow front itself (Figures 5 and 6). Rapid extrusion of lava at ∼2500 m depth has the potential to trap seawater as flows traverse the seafloor, creating conditions for rapid expansion or collapse of newly forming lava morphologies (Engels et al., 2003; Perfit et al., 2003; Soule et al., 2006). Additionally, high flow velocities (∼0.12 m/s in the early stage of the eruption) have been inferred from studies of the CO_2 contents of 2005–2006 lava in this area (Gardner et al., 2016; Graham et al., 2018; Soule et al., 2012). The commonly observed association of lava channels floored with sheet and hackly lava, and the prevalence of lava channels formed during the 2005–2006 eruptions, strongly suggest high flow rates and the transitions of lava channels into tube-fed lobate flows that terminate in pillow fronts (Figures 3, 5, and 6). These observations support the idea that lava-seawater interaction occurs throughout the length of submarine lava flows from their eruptive source at dike-fed fissures out onto the terrain flanking the axis. However, rapid expansion or collapse fail to explain the clusters of acoustic events a few hundred meters upslope from the flow front since the clusters of acoustic events coincide with sheet flows identified by towed camera imagery (Figure 6a, Fundis et al., 2010). An alternative hypothesis for generating impulsive events is the implosion of molten lava (Chadwick et al., 2016). However, observations from Axial Seamount show the implosions also occurred in areas where the lava flow is thick (>5 m). Although the mapping data do not provide conclusive evidence to support either mechanism, impulsive events locations are likely to be a reliable indicator of flow extent. On the west flank of the AST near 9°50.5′N, a cluster of impulsive events can be seen around the edges and beyond the mapped flow extent (Figure 5), which occurred 2–4 days after the main lava emplacement event on 22 January 2006 (Figure 9c). Considering the errors in location of the acoustic events, this spatial relationship and timing of impulsive events might be explained by a gravitational collapse of partially cooled lavas after initial emplacement, which is consistent with the unusually thick lava flow (>9 m) observed at that location.

4.2. Tectonic Discontinuities

Fine-scale tectonic segmentation is commonly observed at fast-spreading MORs like the EPR, and seismic reflection imaging of the AML shows segmentation of the seafloor fissure system (i.e., AST) is strongly controlled

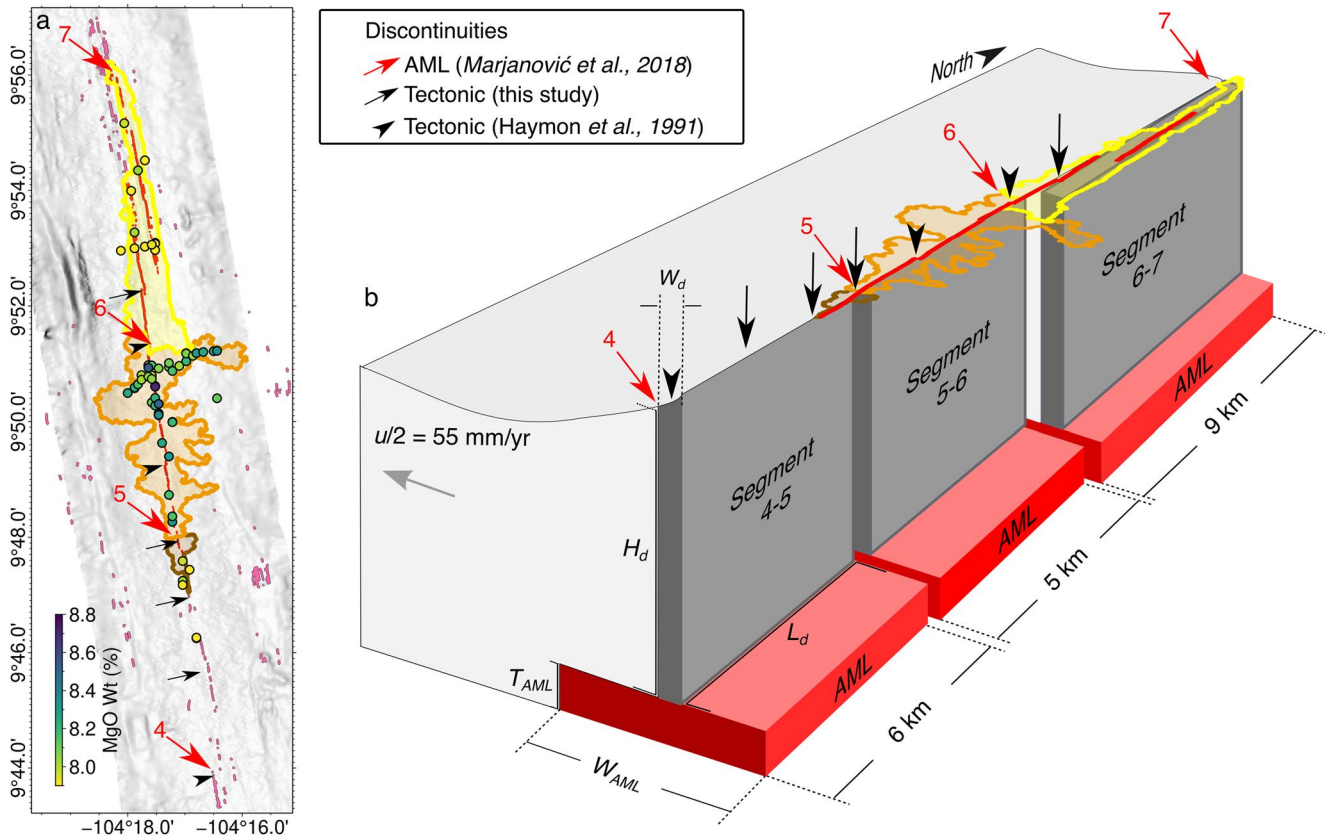

Figure 10. (a) Extent of 2005–2006 eruptions in segments 4–5 (dark orange), 5–6 (orange), and 6–7 (yellow); red numbered arrows are axial magma lens (AML) discontinuities (Marjanović et al., 2018); black arrows with tails are newly identified tectonic discontinuities, arrowheads are previously identified tectonic discontinuities (Haymon et al., 1991; also see Table S1 in Supporting Information S1); circles are basalt glasses shaded by MgO% (Goss et al., 2010); red/pink lines are fissures inside/outside axial summit trough (AST), respectively. (b) Perspective cartoon showing geometry of three rectangular cuboid AML segments used in volume calculation, which likely fed the 2005–2006 eruptions.

by the stress field imparted by partitioning in the magma reservoir located ~1.4–1.6 km below the seafloor (e.g., Carbotte et al., 2013; Fornari et al., 1998; Macdonald et al., 1988; Toomey et al., 2007; White, 2002). At the smallest scale, fourth-order discontinuities are defined by ~50–500 m lateral offsets, or small changes in the width or trend of the AST (e.g., Haymon et al., 1991; Macdonald et al., 1988). Using offsets in the AST as a primary indicator, we identify seven tectonic discontinuities within the area mapped by *Sentry* in 2018–2021 (listed in Table S1 in Supporting Information S1), four of which have not been previously identified, and three of them are also not associated with discontinuities in the AML identified in seismic reflection images (Carbotte et al., 2013; Haymon et al., 1991; Marjanović et al., 2018).

Based upon AML segmentation and spatial variations in lava MgO content, three fourth-order segments, numbered 4–5, 5–6 and 6–7 following Carbotte et al. (2013), are thought to have delivered melt to the surface during the 2005–2006 eruptions (Figure 10). Using overlapping flow relationships, and the location of fissures identified within the AST, we mapped the likely lava extent and volume attributable to each segment (Figure 10), yielding volumes $1 \pm 0.3 \times 10^6$, $13 \pm 4 \times 10^6$, and $8 \pm 3 \times 10^6$ m^3 for segments 4–5, 5–6, and 6–7, respectively (Table 2). The relatively small volume erupted in segment 4–5 may be explained by the presence of four tectonic discontinuities, spaced ~600 m apart with offsets of 60–80 m (Figure 10). These small lateral offsets in the fissure system may serve as evidence that the subsurface discontinuity results in less melt delivery from the finely segmented AML to the surface during eruptive episodes (Carbotte et al., 2013), and may also explain the observed lower MgO content (with respect to adjacent EPR third-order segments) of basaltic glasses formed during the 2005–2006 eruptions, which suggests cooler melt temperatures (Goss et al., 2010).

Table 2
Parameters Used in Volumetric and Eruption Interval Calculations for Segments 4–5, 5–6, and 6–7 During 2005–2006 Eruptions

	Segment 4–5		Segment 5–6		Segment 6–7	
	27% melt extracted		92% melt extracted		27% melt extracted	
	AML thickness, m		AML thickness, m		AML thickness, m	
	10	30	10	30	10	30
V_x, $\times 10^6$ m^3	9.7	29.2	27.6	82.8	14.6	43.7
V_e, $\times 10^6$ m^3	1.0 ± 0.3	1.0 ± 0.3	13.0 ± 4	13.0 ± 4	8.0 ± 3	8.0 ± 3
V_d, $\times 10^6$ m^3	8.7 ± 0.3	28.2 ± 0.3	14.6 ± 4	69.8 ± 4	6.6 ± 3	35.7 ± 3
W_d, m	1.0 ± 0.1	3.2 ± 0.1	1.9 ± 0.6	9.3 ± 0.6	0.5 ± 0.3	2.5 ± 0.3
t_m, yr	9.0 ± 1	29.0 ± 1	18.0 ± 5	85.0 ± 5	4.0 ± 2	23.0 ± 2

Note. V_x is extracted magma volume; V_e is erupted magma volume; V_d is dike volume; W_d is dike width; t_e is eruption interval.

4.3. Melt Content and Dike Width

Three-dimensional multichannel seismic reflection images collected in 2008 provide an insight into the physical properties of the AML following with 2005–2006 eruptions (e.g., Marjanović et al., 2018, 2014; Xu et al., 2014). Estimates of AML thickness vary between 10 and 30 m, and one-dimensional waveform inversion modeling shows that the AML consists of melt-rich and melt-poor segments, with melt contents between 71%–98% and 6%–41%, respectively (Xu et al., 2014). Partial-offset stacks show that segment 5–6 was relatively melt-poor in 2008 and so may have been largely drained during the 2005–2006 eruptions (92% melt extracted maximum), while adjacent segments 4–5 and 6–7 remained melt-rich in 2008, indicating that they were not fully drained (27% melt extracted maximum; Xu et al., 2014). Although there is considerable uncertainty in melt content from these waveform inversion models (30%–92%; Xu et al., 2014), for the maximum extraction scenario, the full width of the AML would be drained, yielding an upper bound on the volume of melt available. In this case, we can combine these estimates with our estimates of surface erupted volume to infer the volume of melt retained within the crust (presumably in dikes) beneath each of the three segments impacted by the 2005–2006 eruptions, and to infer combined dike width and hence repeat time of the eruptive cycle within each segment. For each segment, we estimate the volume of melt extracted from the melt lens, V_x, assuming a simple rectangular cuboid AML geometry (Figure 10), using

$$V_x = f W_{\mathrm{AML}} T_{\mathrm{AML}} L_{\mathrm{AML}} \quad (2)$$

where f is melt fraction, while W_{AML}, T_{AML}, and L_{AML} are AML width, thickness, and length (600 ± 100 m, 20 ± 10 m, and 5,000–9,000 ± 200 m respectively), estimates of which are taken from Xu et al. (2014). Assuming a most-likely AML thickness of 10 m (Xu et al., 2014), we obtain a maximum estimate of combined volume extracted across the three segments of 51.9 × 10^6 m^3. Subtracting our erupted volume estimate, $V_e = 22.4 \pm 7 \times 10^6$ m^3, from V_x, we estimate that a combined volume, V_d, of ~29.5 ± 7 × 10^6 m^3 of melt remained in the subsurface following the eruption, presumably as a single or multiple dikes, representing ~57% of the total melt extracted from the three AML segments. Assuming a 10 m-thick AML and simple single-dike case, and taking the height of the dike, H_d, to be the distance between the AML and the seafloor (ranging from 1,465 to 1,615 m; Marjanović et al., 2018), and assuming that dike length, L_d, is equal to the distance between AML discontinuities, we obtain dike width, W_d, estimates of 1.0 ± 0.1, 1.9 ± 0.6, and 0.5 ± 0.3 m for segments 4–5, 5–6 and 6–7, respectively (Figure 10 and Table 2). These dike width estimates, with an AML thickness of 10 m, are comparable to the mean dike width (0.5–2 m) observed at ophiolites and inferred from CO_2 content (Gardner et al., 2016; Gudmundsson, 1995; Harper, 1984; Kidd, 1977; Rosencrantz, 1983; Umino et al., 2003). In contrast, for an AML thickness of 30 m, resulting dike width estimates range from 2.5 to 9.3 m, which is not consistent with field observations elsewhere and is hence less likely. Alternatively, if we assume that the dike only intrudes beneath the fissures, dike length can be estimated from the total length of fissures mapped on the seafloor. Using this approach and assuming an AML thickness of 10 m, we estimate a dike width of 1.8 ± 0.1 m, 2.5 ± 0.6 m, and 0.6 ± 0.3 m for segments 4–5, 5–6 and 6–7, respectively, which is broadly similar to the more simple approach assuming a continuous dike between AML discontinuities.

Assuming that all plate separation is accommodated by episodic dike intrusions, we can use our dike width estimates to infer the magmatic episode time interval, t_m, that would be required to sustain the observed average full spreading rate, u, of 110 mm/yr (Carbotte & Macdonald, 1992) using

$$t_m = \frac{(V_x - V_e)}{L_d H_d u}. \quad (3)$$

For segment 5–6, we obtain a magmatic episode time interval of ∼18 ± 5 years (Table 2), which is comparable to the eruption interval of 14–15 years between the 1991–1992 and 2005–2006 eruptions, and in close agreement with the 20-year time interval estimated by Xu et al. (2014). This slightly longer eruption interval could be explained as a consequence of the 1991–1992 eruptions, which are thought to have been 4–5 times smaller in volume than the 2005–2006 eruptions (Gregg & Fink, 1995). In contrast, we estimate a magmatic episode interval of 9 ± 1 and 4 ± 2 years for segments 4–5, 6–7, respectively. The shorter interval could imply frequent diking events occurring without a detectable volume erupted at the surface. Several linear pillow mounds (∼6 m high, ∼12 m wide, and ∼130 m along-axis length), similar to features found on the Axial Seamount south rift zone after the 2011 eruption, are visible within the AST of segment 4–5 (near 9°46′N, see Figure 6i), supporting the notion that low-effusion-rate eruptions or diking events could have occurred (Chadwick et al., 2013; Clague et al., 2017). Alternatively, a greater proportion of plate spreading could be accommodated by slip on extensional faults in segments 4–5 and 6–7 than in segment 5–6. If the eruption interval of 18 years is uniform across all three segments, then 50%–75% of plate spreading would need to be accommodated by faulting at segments 4–5 and 6–7 in order to make up for the inferred deficit in spreading accommodated by dike intrusion. Although such a high degree of fault-accommodated spreading is unlikely in such a high magma-supply and spreading rate ridge segment (e.g., Buck et al., 2005; Olive & Dublanchet, 2020), faulting may play a role when considered over multiple eruptive cycles, although earthquake data to test this idea are not yet available. A more likely explanation is that over longer time scales than the ∼30 years of observations at the EPR 9°50′N system, magmatic events occur episodically (i.e., at irregular time intervals), and that magmatic episode time interval varies between segments. Hence although segment 5–6 may have undergone eruptions at 15–18 year intervals in the past two cycles, this interval may not have been constant in the past, and although segments 4–5 and 6–7 experienced a shorter time interval with smaller erupted volumes, they may have behaved differently in previous magmatic episodes.

5. Conclusions

We present near-bottom multibeam bathymetric and sidescan sonar data acquired in 2018–2021 during 19 AUV *Sentry* dives, which cover 115 km^2 over the area impacted by the 2005–2006 eruptions at the EPR near 9°50′N. The data reveal meter-scale volcanic seafloor morphology including individual eruptive fissures, vent chimneys, fault scarps, and lava flow types, and allow us to resolve the location of individual features visited with ROV *Jason* in 2021 with an absolute accuracy of <10 m. Combining pre- and post-eruption near-bottom data with impulsive acoustic events recorded during the 2005–2006 eruptions, we determine that the area covered by the eruptions is ∼50% larger than previously thought, although on average the flows are only ∼1 m thick, yielding a total erupted volume of 22.4 ± 7 × 10^6 m^3. Lava flow thickness varies from ∼0.9 m near eruptive fissures up to ∼1.9 m at lava flow margins, a pattern which is in broad agreement with previous interpretations of lava morphology based on near-bottom imagery. Combining previous estimates of AML geometry and melt content with our erupted volume estimates for three separate segments impacted by the 2005–2006 eruptions, we find that 57% of the estimated melt content of the AML likely remained in the subsurface, and that the magmatic episode time interval varies between adjacent segments, from as short as 4 years, up to 18 years. The more frequent interval might imply that frequent diking events occur without emplacing lava on the seafloor, although over longer time periods the magmatic episode time interval is likely to be more uniform in order to accommodate total plate separation. The precisely navigated mapping data presented here provide absolute positional locations for a suite of important hydrothermal vent sites in the study area, and also represent the quantitative baseline necessary to assess the scale and impact of future eruptions at the EPR 9°50′N study area.

Data Availability Statement

Multibeam bathymetric and sidescan sonar data collected by AUV *Sentry*, and fault, fissures, and 2005–2006 flow margin outline shapefiles are available at the Marine Geoscience Data System, at https://doi.org/10.26022/IEDA/330373, https://doi.org/10.26022/IEDA/330374, and https://doi.org/10.26022/IEDA/330841.

Acknowledgments
The authors thank the ships' crews, *Sentry*, *Alvin* and *Jason* teams and scientific parties during cruises AT42-06, AT42-21 and RR2102 for their excellent work. They thank Bill Chadwick and an anonymous reviewer for their insightful comments, and Zoe Yin for help with hydrothermal vent site locations. The figures in study are plotted with Generic Mapping Tools 6 (Wessel et al., 2019). This project is supported by National Science Foundation grants OCE-1834797, OCE-1949485, OCE-194893, OCE-1949938, and by Scripps Institution of Oceanography's David DeLaCour Endowment Fund.

References

Aghaei, O., Nedimovic, M. R., Carton, H., Carbotte, S. M., Canales, J. P., & Mutter, J. C. (2014). Crustal thickness and Moho character of the fastspreading East Pacific Rise from 9°42′N to 9°57′N from poststack-migrated 3-D MCS data. *Geochemistry, Geophysics, Geosystems*, *15*(3), 634–657. https://doi.org/10.1002/2013GC005069

Barreyre, T., Parnell-Turner, R., Wu, J.-N., Fornari, D. J. (2022). Tracking crustal permeability and hydrothermal response during seafloor eruptions at the East Pacific Rise, 9°50′N. *Geophysical Research Letters* (pp. V31B–05). https://doi.org/10.1029/2021gl095459

Buck, W. R., Lavier, L., & Poliakov, A. N. B. (2005). Modes of faulting at mid-ocean ridges. *Nature*, *434*, 719–723. https://doi.org/10.1038/nature03358

Canales, J. P., Carton, H., Carbotte, S. M., Mutter, J. C., Nedimović, M. R., Xu, M., et al. (2012). Network of off-axis melt bodies at the East Pacific Rise. *Nature Geoscience*, *5*, 279–283. https://doi.org/10.1038/ngeo1377

Carbotte, S. M., & Macdonald, K. C. (1992). East Pacific Rise 8°–10°30′N: Evolution of ridge segments and discontinuities from SeaMARC II and three-dimensional magnetic studies. *Journal of Geophysical Research*, *97*(B5), 6959. https://doi.org/10.1029/91jb03065

Carbotte, S. M., Marjanović, M., Carton, H., Mutter, J. C., Canales, J. P., Nedimovi, M. R., et al. (2013). Fine-scale segmentation of the crustal magma reservoir beneath the East Pacific Rise. *Nature Geoscience*, *6*(10), 866–870. https://doi.org/10.1038/ngeo1933

Caress, D., Clague, D. A., Paduan, J. B., Martin, J. F., Dreyer, B. M., Chadwick, W. W., et al. (2012). Repeat bathymetric surveys at 1-metre resolution of lava flows erupted at Axial Seamount in April 2011. *Nature Geoscience*, *5*(7), 483–488. https://doi.org/10.1038/ngeo1496

Chadwick, W., Clague, D. A., Embley, R. W., Perfit, M. R., Butterfield, D. A., Caress, D. W., et al. (2013). The 1998 eruption of Axial Seamount: New insights on submarine lava flow emplacement from high-resolution mapping. *Geochemistry, Geophysics, Geosystems*, *14*(10), 3939–3968. https://doi.org/10.1002/ggge.20202

Chadwick, W., Embley, R. W., & Fox, C. G. (1991). Evidence for volcanic eruption on the southern Juan de Fuca ridge between 1981 and 1987. *Nature*, *350*(April), 416–418.

Chadwick, W., Paduan, J. B., Clague, D. A., Dreyer, B. M., Merle, S. G., Bobbitt, A. M., et al. (2016). Voluminous eruption from a zoned magma body after an increase in supply rate at Axial Seamount. *Geophysical Research Letters*, *43*(23), 12063–12070. https://doi.org/10.1002/2016GL071327

Chadwick, W., Scheirer, D. S., Embley, R. W., & Johnson, H. P. (2001). Highresolution bathymetric surveys using scanning sonars: Lava flow morphology, hydrothermal vents, and geologic structure at recent eruption sites on the Juan de Fuca Ridge. *Journal of Geophysical Research: Solid Earth*, *106*(B8), 16075–16099. https://doi.org/10.1029/2001jb000297

Chadwick, W. W., Jr, Cashman, K. V., Embley, R. W., Matsumoto, H., Dziak, R. P., de Ronde, C. E. J., et al. (2008). Direct video and hydrophone observations of submarine explosive eruptions at NW Rota-1 volcano, Mariana arc. *Journal of Geophysical Research: Solid Earth*, *113*, B08S10. https://doi.org/10.1029/2007JB005215

Chadwick, W. W., Jr, Rubin, K. H., Merle, S. G., Bobbitt, A. M., Kwasnitschka, T., & Embley, R. W. (2019). Recent eruptions between 2012-2018 discovered at West Mata submarine volcano (NE Lau Basin, SW Pacific) and characterized by new ship, AUV, and ROV data. *Frontiers in Marine Science*, *6*, 495. https://doi.org/10.3389/fmars.2019.00495

Clague, D., Paduan, J., Caress, D., Chadwick, W., Le Saout, M., Dreyer, B., & Portner, R. (2017). High-resolution AUV mapping and targeted ROV observations of three historical lava flows at axial Seamount. *Oceanography*, *30*(4). https://doi.org/10.5670/oceanog.2017.426

Colman, A., Sinton, J. M., White, S. M., McClinton, J. T., Bowles, J. A., Rubin, K. H., et al. (2012). Effects of variable magma supply on mid-ocean ridge eruptions: Constraints from mapped lava flow fields along the Galápagos Spreading Center. *Geochemistry, Geophysics, Geosystems*, *13*(8). https://doi.org/10.1029/2012GC004163

Cowen, J. P., Fornari, D. J., Shank, T. M., Love, B., Glazer, B. H., Treusch, A. H., et al. (2007). Volcanic eruptions at East Pacific Rise near 9°50′ north. *Eos Transactions - American Geophysical Union*, *88*(7), 81–83.

Crisp, J. A. (1984). Rates of magma emplacement and volcanic output. *Journal of Volcanology and Geothermal Research*, *20*, 177–211.

Detrick, R. S., Buhl, P., Vera, E., Mutter, J., Orcutt, J., Madsen, J., & Brocher, T. (1987). Multi-channel seismic imaging of a crustal magma chamber along the East Pacific Rise. *Nature*, *326*(6108), 35–41. https://doi.org/10.1038/326035a0

Engels, J. L., Edwards, M. H., Fornari, D. J., Perfit, M. R., & Cann, J. R. (2003). A new model for submarine volcanic collapse formation. *Geochemistry, Geophysics, Geosystems*, *4*(9), 1–22. https://doi.org/10.1029/2002GC000483

Ferrini, V. L., Fornari, D. J., Shank, T. M., Kinsey, J. C., Tivey, M., Soule, S. A., et al. (2007). Submeter bathymetric mapping of volcanic and hydrothermal features on the East Pacific Rise crest at 9°50′N. *Geochemistry, Geophysics, Geosystems*, *8*(1). https://doi.org/10.1029/2006GC001333

Feuillet, N., Jorry, S., Crawford, W. C., Deplus, C., Thinon, I., Jacques, E., et al. (2021). Birth of a large volcanic edifice offshore Mayotte via lithosphere-scale dyke intrusion. *Nature Geoscience*, *14*, 787–795. https://doi.org/10.1038/s41561-021-00809-x

Fornari, D. J., Haymon, R. M., Perfit, M. R., Gregg, T. K. P., & Edwards, M. H. (1998). Axial summit trough of the East Pacific Rice 9-10N: Geological characteristics and evolution of the axial zone on fast spreading mid-ocean ridge. *Journal of Geophysical Research: Solid Earth*, *103*(B5), 9827–9855. https://doi.org/10.1029/98jb00028

Fornari, D. J., Tivey, M., Schouten, H., Perfit, M., Yoerge, D., Bradley, A., et al. (2004). Submarine lava flow emplacement at the east pacific rise 9°50′N: Implications for uppermost ocean crust stratigraphy and hydrothermal fluid circulation. In C. R. German, & L. M. Parson (Eds.), *Mid-ocean ridges: Hydrothermal interactions between the lithosphere and oceans, geophysical monograph series* (pp. 187–217). American Geophysical Union. https://doi.org/10.1029/148GM08

Fornari, D. J., Von Damm, K. L., Bryce, J. G., Cowen, J. P., Ferrini, V., Fundis, A., et al. (2012). The East Pacific Rise between 9°N and 10°N: Twenty-five years of integrated, multidisciplinary oceanic spreading center studies. *Oceanography*, *25*(1), 18–43. https://doi.org/10.5670/oceanog.2012.02

Fox, C. G., Chadwick, W. W., & Embley, R. W. (1992). Detection of changes in ridge-crest morphology using repeated multibeam sonar surveys. *Journal of Geophysical Research*, *97*, 11149–11162.

Fundis, A. T., Soule, S. A., Fornari, D. J., & Perfit, M. R. (2010). Paving the seafloor: Volcanic emplacement processes during the 2005-2006 eruptions at the fast spreading East Pacific Rise, 9°50′N. *Geochemistry, Geophysics, Geosystems*, *11*(8). https://doi.org/10.1029/2010GC003058

Gardner, J. E., Jackson, B. A., Gonnermann, H., & Soule, S. A. (2016). Rapid ascent and emplacement of basaltic lava during the 2005–06 eruption of the East Pacific Rise at ca. 9°51′N as inferred from CO_2 contents. *Earth and Planetary Science Letters*, *453*, 152–160. https://doi.org/10.1016/j.epsl.2016.08.007

Goss, A. R., Perfit, M. R., Ridley, W. I., Rubin, K. H., Kamenov, G. D., Soule, S. A., et al. (2010). Geochemistry of lavas from the 2005–2006 eruption at the East Pacific Rise, 9°46′N–9°56′N: Implications for ridge crest plumbing and decadal changes in magma chamber compositions. *Geochemistry, Geophysics, Geosystems*, *11*(5), 1–35. https://doi.org/10.1029/2009GC002977

Graham, D. W., Michael, P. J., & Rubin, K. H. (2018). An investigation of mid-ocean ridge degassing using He, CO_2, and $\delta^{13}C$ variations during the 2005–06 eruption at 9°50′N on the East Pacific Rise. *Earth and Planetary Science Letters*, *504*, 84–93. https://doi.org/10.1016/j.epsl.2018.09.040

Gregg, T. K., & Fink, J. H. (1995). Quantification of submarine lava-flow morphology through analog experiments. *Geology*, *23*(1), 73–76. https://doi.org/10.1130/0091-7613(1995)023h0073:QOSLFMi2.3.CO

Gudmundsson, A. (1995). The geometry and growth of dykes. In R. Balkema (Ed.), *Physics and chemistry of dykes* (pp. 23–34).

Han, S., Carbotte, S. M., Carton, H., Mutter, J. C., Aghaei, O., Nedimović, M. R., et al. (2014). Architecture of on- and off-axis magma bodies at EPR 9°37–40′N and implications for oceanic crustal accretion. *Earth and Planetary Science Letters*, *390*, 31–44. https://doi.org/10.1016/j.epsl.2013.12.040

Harding, A. J., Kent, G. M., & Orcutt, J. A. (1993). A multichannel seismic investigation of upper crustal structure at 9°N on the East Pacific Rise: Implications for crustal accretion. *Journal of Geophysical Research*, *98*(B8), 925–944. https://doi.org/10.1029/93jb00886

Harper, G. D. (1984). The Josephine ophiolite, northwestern California. *The Geological Society of America Bulletin*, *95*(9), 1009–1026. https://doi.org/10.1130/0016-7606(1984)95<1009:TJONC>2.0.CO;2

Haymon, R. M., Fornari, D. J., Edwards, M. H., Carbotte, S., Wright, D., & Macdonald, K. C. (1991). Hydrothermal vent distribution along the East Pacific Rise crest (9°9′–54′N) and its relationship to magmatic and tectonic processes on fast-spreading mid-ocean ridges. *Earth and Planetary Science Letters*, *104*(2–4), 513–534. https://doi.org/10.1016/0012-821X(91)90226-8

Haymon, R. M., Fornari, D. J., Von, K. L. D., Lilley, M. D., Perfit, M., Edmond, J. M., et al. (1993). Volcanic eruption of the mid-ocean ridge along the East Pacific Rise crest at 9°45–52′N: Direct submersible observations of seafloor phenomena associated with an eruption event in April, 1991. *Earth and Planetary Science Letters*, *119*, 85–101. https://doi.org/10.1016/0012-821X(93)90008-W

Humphris, S. E., Zierenberg, R. A., Mullineaux, L. S., & Thomson, R. E. (Eds.), (1995). *Seafloor hydrothermal systems: Physical, chemical, biological, and geological interactions (No. 91)*. American Geophysical Union.

Kidd, R. G. (1977). A model for the process of formation of the upper oceanic crust. *Geophysical Journal of the Royal Astronomical Society*, *50*(1), 149–183. https://doi.org/10.1111/j.1365-246X.1977.tb01328.x

Macdonald, K. C., & Fox, P. J. (1988). The axial summit graben and cross-sectional shape of the East Pacific Rise as indicators of axial magma chambers and recent volcanic eruptions. *Earth and Planetary Science Letters*, *88*(1–2), 119–131. https://doi.org/10.1016/0012-821X(88)90051-9

Macdonald, K. C., Fox, P. J., Perram, L. J., Eisen, M. F., Haymon, R. M., Miller, S. P., et al. (1988). A new view of the mid-ocean ridge from the behaviour of ridge-axis discontinuities. *Nature*, *335*(6187), 217–225. https://doi.org/10.1038/335217a0

Marjanović, M., Carbotte, S. M., Carton, H., Nedimović, M. R., Canales, J. P., & Mutter, J. C. (2018). Crustal magmatic system beneath the east Pacific Rise: Implications for tectonomagmatic segmentation and crustal melt transport at fast-spreading Ridges. *Geochemistry, Geophysics, Geosystems*, *19*, 4584–4611. https://doi.org/10.1029/2018GC007590

Marjanović, M., Carbotte, S. M., Carton, H., Nedimović, M. R., Mutter, J. C., & Canales, J. P. (2014). A multi-sill magma plumbing system beneath the axis of the East Pacific Rise. *Nature Geoscience*, *7*(11), 825–829. https://doi.org/10.1038/ngeo2272

Mutter, J. C., Barth, G. A., Buhl, P., Detrick, R. S., Orcutt, J., & Harding, A. (1988). Magma distribution across ridge-axis discontinuities on the East Pacific Rise from multichannel seismic images. *Nature*, *336*(6195), 156–158. https://doi.org/10.1038/336156a0

Olive, J. A., & Dublanchet, P. (2020). Controls on the magmatic fraction of extension at mid-ocean ridges. *Earth and Planetary Science Letters*, *549*, 116541. https://doi.org/10.1016/j.epsl.2020.116541

Orcutt, J. A., Kennett, B. L., & Dorman, L. R. M. (1976). Structure of the East Pacific Rise from an ocean bottom seismometer survey. *Geophysical Journal of the Royal Astronomical Society*, *45*(2), 305–320. https://doi.org/10.1111/j.1365-246X.1976.tb00328.x

Perfit, M. R., Cann, J. R., Fornari, D. J., Engels, J., Smith, D. K., Ridley, W. I., & Edwards, M. H. (2003). Interaction of sea water and lava during submarine eruptions at mid-ocean ridges. *Nature*, *426*(6962), 62–65. https://doi.org/10.1038/nature02032

Pyle, D. M. (2015). Sizes of volcanic eruptions. In H. Sigurdsson (Ed.), *The encyclopedia of volcanoes*. Academic Press. https://doi.org/10.1016/b978-0-12-385938-9.00013-4

Rosencrantz, E. (1983). The structure of sheeted dikes and associated rocks in North Arm massif, Bay of Islands ophiolite complex, and the intrusive process at oceanic spreading centers. *Canadian Journal of Earth Sciences*, *20*(5), 787–801. https://doi.org/10.1139/e83-070

Rubin, K. H., Perfit, M. R., Fornari, D. J., Soule, S. A., Tolstoy, M. & Waldhauser, F. (2006). Geochronology and composition of the 2005–06 volcanic Eruptions of the East Pacific Rise, 9°46′–56′N. Abstract V23B-0602 presented at AGU Fall Meeting, San Francisco, Calif., Dec. 11–16.

Rubin, K. H., Soule, S. A., Chadwick, W. W., Fornari, D. J., Clague, D. A., Embley, R. W., et al. (2012). Volcanic eruptions in the deep sea. *Oceanography*, *25*(1), 143–157. https://doi.org/10.5670/oceanog.2012.12

Rubin, K. H., Tolstoy, M., Fornari, D. J., Dziak, R. P., Soule, S. A., Waldhauser, F. & von Damm, K. L. (2008). Integrating radiometric, geophysical and thermal signals of volcanic unrest and eruption in 2005–06 at 9°50′N EPR. Abstract B23F-07 presented at AGU Fall Meeting, San Francisco, Calif., Dec. 15–19.

Sinton, J. (2002). Volcanic eruptions on mid-ocean ridges: New evidence from the superfast spreading East Pacific Rise, 17°–19°S. *Journal of Geophysical Research*, *107*(B6). https://doi.org/10.1029/2000jb000090

Sinton, J., & Detrick, R. S. (1992). Mid-ocean ridge magma chambers. *Journal of Geophysical Research*, *97*(B1), 197–216. https://doi.org/10.1029/91JB02508

Soule, S. A., Ferrini, V. L., Kinsey, J. C., Fornari, D. J., Sellers, C., White, S. M., et al. (2008). Navigational infrastructure at the East Pacific Rise 9°50′N area following the 2005–2006 eruption: Seafloor benchmarks and near-bottom multibeam surveys. *Geochemistry, Geophysics, Geosystems*, *9*(11), 1–13. https://doi.org/10.1029/2008GC002070

Soule, S. A., Fornari, D. J., Perfit, M. R., Ridley, W. I., Reed, M. H., & Cann, J. R. (2006). Incorporation of seawater into mid-ocean ridge lava flows during emplacement. *Earth and Planetary Science Letters*, *252*(3–4), 289–307. https://doi.org/10.1016/j.epsl.2006.09.043

Soule, S. A., Fornari, D. J., Perfit, M. R., & Rubin, K. H. (2007). New insights into mid-ocean ridge volcanic processes from the 2005–2006 eruption of the East Pacific Rise, 9°46′N–9°56′N. *Geology*, *35*(12), 1079–1082. https://doi.org/10.1130/G23924A.1

Soule, S. A., Nakata, D. S., Fornari, D. J., Fundis, A. T., Perfit, M. R., & Kurz, M. D. (2012). CO_2 variability in mid-ocean ridge basalts from syn-emplacement degassing: Constraints on eruption dynamics. *Earth and Planetary Science Letters*, *327–328*, 39–49. https://doi.org/10.1016/j.epsl.2012.01.034

Tan, Y. J., Tolstoy, M., Waldhauser, F., & Wilcock, W. S. (2016). Dynamics of a seafloor-spreading episode at the East Pacific Rise. *Nature*, *540*(7632), 261–265. https://doi.org/10.1038/nature20116

Tolstoy, M., Cowen, J. P., Baker, E. T., Fornari, D. J., Rubin, K. H., Shank, T. M., et al. (2006). A sea-floor spreading event captured by seismometers. *Science*, *314*(5807), 1920–1922. https://doi.org/10.1126/science.1133950

Tolstoy, M., Waldhauser, F., Bohnenstiehl, D. R., Weekly, R. T., & Kim, W. Y. (2008). Seismic identification of along-axis hydrothermal flow on the East Pacific Rise. *Nature*, *451*(7175), 181–184. https://doi.org/10.1038/nature06424

Toomey, D. R., Jousselin, D., Dunn, R. A., Wilcock, W. S., & Detrick, R. S. (2007). Skew of mantle upwelling beneath the East Pacific Rise governs segmentation. *Nature*, *446*(7134), 409–414. https://doi.org/10.1038/nature05679

Umino, S., Miyashita, S., Hotta, F., & Adachi, Y. (2003). Along-strike variation of the sheeted dike complex in the Oman Ophiolite: Insights into subaxial ridge segment structures and the magma plumbing system. *Geochemistry, Geophysics, Geosystems*, *4*(9). https://doi.org/10.1029/2001GC000233

Vergniolle, S., Brandeis, G., & Mareschal, J. C. (1996). Strombolian explosions 2. Eruption dynamics determined from acoustic measurements. *Journal of Geophysical Research B: Solid Earth*, *101*(9), 20449–20466. https://doi.org/10.1029/96jb01925

Wessel, P., Luis, J. F., Uieda, L., Scharroo, R., Wobbe, F., Smith, W. H. F., & Tian, D. (2019). The generic mapping Tools version 6. *Geochemistry, Geophysics, Geosystems*, *20*, 5556–5564. https://doi.org/10.1029/2019GC008515

White, S. M. (2002). Correlation between volcanic and tectonic segmentation of fast-spreading ridges: Evidence from volcanic structures and lava flow morphology on the East Pacific Rise at 910N. *Journal of Geophysical Research*, *107*(B8). https://doi.org/10.1029/2001jb000571

White, S. M., Haymon, R. M., & Carbotte, S. (2006). A new view of ridge segmentation and near-axis volcanism at the East Pacific Rise, 8°-12°N, from EM300 multibeam bathymetry. *Geochemistry, Geophysics, Geosystems*, *7*(12). https://doi.org/10.1029/2006GC001407

Wilcock, W. S. D., Dziak, R. P., Tolstoy, M., Chadwick, W. W., Nooner, S. L., Bohnenstiehl, D. W. R., et al. (2018). The recent volcanic history OF axial seamount: Geophysical insights into past eruption dynamics with an eye toward enhanced observations of future eruptions. *Oceanography*, *31*, 114–123. https://doi.org/10.5670/oceanog.2018.117

Wilcock, W. S. D., Tolstoy, M., Waldhauser, F., Garcia, C., Tan, Y. J., Bohnenstiehl, D. R., et al. (2016). Seismic constraints on caldera dynamics from the 2015 AxialSeamount eruption. *Science*, *354*(6318), 1395–1399. https://doi.org/10.1126/science.aah5563

Wright, D. J., Haymon, R. M., & Fornari, D. J. (1995). Crustal fissuring and its relationship to magmatic and hydrothermal processes on the East Pacific Rise crest (9°12′ to 54′N). *Journal of Geophysical Research*, *100*(B4), 6097–6120. https://doi.org/10.1029/94JB02876

Xu, M., Pablo Canales, J., Carbotte, S. M., Carton, H., Nedimovic, M. R., & Mutter, J. C. (2014). Variations in axial magma lens properties along the East Pacific Rise (9°30′N-10°00′N) from swath 3-D seismic imaging and 1-D waveform inversion. *Journal of Geophysical Research: Solid Earth*, *119*(4), 2721–2744. https://doi.org/10.1002/2013JB010730

References From the Supporting Information

Caress, D., & Chayes, D. N. (1996). Improved processing of hydrosweep DS multibeam data on the R/V Maurice Ewing. *Marine Geophysical Researches*, *18*(6), 631–650. https://doi.org/10.1007/BF00313878

Caress, D., Thomas, H., Kirkwood, W., McEwen, R., Henthorn, R., Clague, D., et al. (2008). High-resolution multibeam, sidescan, and subbottom surveys using the MBARI AUV D. Allan B. *Marine habitat mapping technology for Alaska* (pp. 47–70). https://doi.org/10.4027/mhmta.2008.04

Chen, H. H. (2008). In-situ alignment calibration of attitude and ultra short baseline sensors for precision underwater positioning. *Ocean Engineering*, *35*(14–15), 1448–1462. https://doi.org/10.1016/j.oceaneng.2008.06.013

Dhanak, M. R., & Xiros, N. I. (2016). *Handbook of ocean engineering*. Springer US. https://doi.org/10.1007/978-3-319-16649-0

Egbert, G. D., & Erofeeva, S. Y. (2002). Efficient inverse modeling of barotropic ocean tides. *Journal of Atmospheric and Oceanic Technology*, *19*(2), 183–204. https://doi.org/10.1175/1520-0426(2002)019h0183

Kinsey, J. C., Eustice, R. M., & Whitcomb, L. L. (2006). A survey of underwater vehicle navigation: Recent advances and new challenges. In *Conf. manoeuvering control marine craf* (pp. 1–12). https://doi.org/10.1007/978-3-319-47766-418

Stutters, L., Liu, H., Tiltman, C., & Brown, D. J. (2008). Navigation technologies for autonomous underwater vehicles. *IEEE Transactions on Systems, Man, and Cybernetics - Part C: Applications and Reviews*, *38*(4), 581–589. https://doi.org/10.1109/TSMCC.2008.919147